Electronic Laser Photodissociation Spectroscopy of Gas-Phase Metalloporphyrins and Metalloporphyrin-Aromatic Molecule Complexes

Mathew Hawkridge

Master of Science by Research

University of York

Chemistry

November 2017

Abstract

Metal containing porphyrins are found in crude oil at concentrations of 100-1000 PPM. Their presence can pose a challenge to petroleum chemistry as they poison hydrocarbon cracking catalysts, complicating the upcycling of heavy, long-chain petroleum. In this thesis, the electronic spectroscopy and photochemistry of isolated, gaseous metalloporphyrins, along with measurements for gas-phase metalloporphyrin-aromatic molecule complexes is studied. The electronic spectroscopic properties of; iron, nickel and vanadium tetraphenyl porphyrin, as well the unmetallated tetraphenyl porphyrin and hemin are studied, to provide information on how the metal centre and functional groups influence the intrinsic electronic spectra. In particular, the position, width and intensity of the two key porphyrin absorption bands, the "Soret" and Q bands is explored. Further experiments focus on metalloporphyrin-aromatic molecule clusters (e.g. pyridine and quinoline) to probe the effect of direct axial coordination to the metal centre on the electronic spectrum. The gaseous metalloporphyrins and their clusters have been studied in a novel custom-adapted laser-interfaced commercial mass spectrometer, where they are produced via electrospray ionization, mass-selected and then subjected to laser photoexcitation within a quadrupole ion trap, allowing the photochemistry to be monitored as a function of excitation wavelength. The results presented in this work represent the first direct measurements of the photodegradation pathways of metalloporphyrins and their complexes.

Contents

List of Tables

Chapter 4

Chapter 5

Appendix

List of Figures

Chapter 1: Introduction

Chapter 2: Background Theory

Chapter 3: Tetraphenyl Porphyrin

Chapter 4: Metalloporphyrins

Chapter 5: Metalloporphyrin Complexes

Appendix

Acknowledgements

I would firstly like to thank Caroline for her help in the research and the writing of this thesis. I would also like to thank the Dessent research group, especially Ed and Rosaria for their help and input with this work

Declaration

I declare that this thesis is a presentation of original work and I am the sole author.

This work has not previously been presented for an award at this, or any other

University. All sources are acknowledged as References.

Chapter 1: Introduction

1.1 Porphyrins

Porphyrins belong to a class of molecules that are ubiquitous throughout the natural world. They are a macrocyclic aromatic system consisting of 4 pyrrole units joined by 4 methine groups that can be substituted in many different ways, with the simplest structure known as porphin. The central cavity is known for being able to bind many different metals, forming a metalloporphyrin (MP). These metallated porphyrins are of interest in many different areas of chemistry, such as acting as photosensitizers to improve efficiency of catalysts. [1] Dye-sensitized solar cells are also a particular area of intense research. [2-4] Additionally they have found use in pharmaceutical applications, with the drug Verteporfin used in photodynamic therapy, where it acts as a singlet oxygen producer to remove abnormal blood vessels associated with macular degeneration. [5,6]

MPs are perhaps best known however for the crucial roles they play in biological systems. Of these, the most notable are the iron centred heme porphyrin, which is used in oxygen transport for all vertebrates, and the magnesium centred chlorophyll molecule that is central to photosynthesis. Much ongoing research is focused on forming synthetic mimics of these two molecules due to their importance in biology. It is this widespread biological abundance of porphyrins that leads to them being of interest to geochemists. As shown by Treibs in the 1930's, [7-10] and further investigated by Dunning in the 1950's, [11-13] fossil fuels are formed from the

decomposed organic matter of biological systems. Whilst almost all biological structure is lost in this process, the porphyrin molecules are retained as largely intact structures, although chemically modified by the process. The biologically present iron and magnesium metal centres are typically replaced with more inert nickel and vanadium ones. In addition, the long-functionalised side chains, such as those found in the chlorophyll system are lost, replaced by short hydrocarbon chains or benzene rings.[14] These resultant structures are known as geoporphyrins, and are present at approximately 100-1000 PPM in most oil.[15, 16] This geological conversion is summarised in Figure 1.1.

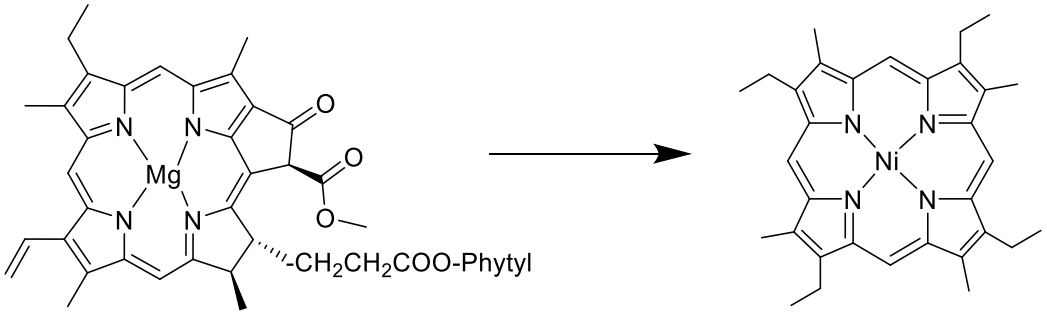

Figure 1.1. *A typical geochemical conversion, where the more complex chlorophyll A is transformed into a nickel etioporphyrin, a commonly found geoporphyrin in crude oil.*

Geoporphyrin presence has been exploited in oil exploration, as the ratio and quantity of the various porphyrins can be used to gain geochemical information, such as the age of the oil and the location of the source rock of the oil. [17]

These MPs however also pose a significant challenge to petroleum science, since their presence, even at low concentrations, can adversely affect the performance of hydrocarbon cracking catalysts routinely used in petroleum processing. This can lead to certain sources of oil being unusable.[16-18] The reason for this is that the MPs deposit their metal ion onto the zeolite catalysts used in cracking reactions. Nickel

for example, is deposited onto the surface of the catalyst as nickel oxide and then subsequently reduced to nickel. Instead of cracking the oil, nickel catalyses dehydrogenation of oil which forms hydrogen gas and coke (carbon rich deposits). This decreases the turnover rate of the catalyst, and lowers the yield of desired cracked oil produced. [17, 20, 21]

The most in demand fractions of hydrocarbons that are extracted from crude oil are those that are lighter and have a lower boiling point. These species are distilled off from the crude, leaving behind heavier, higher boiling point fractions. The ever-increasing demand for light petroleum has made the conversion of these heavy fractions into lighter fractions by cracking a key process in petroleum refinement.

It is well accepted that MPs are predominantly found in the heavier, higher boiling point fractions of crude oil. [17] Distillation to remove the lighter fractions only serves to enrich their concentration in the remaining oil that needs to be cracked. More specifically, the MPs themselves are found in asphaltene molecules in the heavy fractions. [17,22,23,] These are one of the major heavy components of oil which are defined by their solubility in toluene and insolubility in n-heptane. They consist of complex mixtures of thousands of different molecular species containing carbon, hydrogen, oxygen and sulfur. Whilst their individual structure can vary enormously, they typically have a central unit made up of multiple aromatic and heteroaromatic rings, with long alkyl side chains on the outside. The mass range varies from 400 to several thousand Da, although clear boundaries do not exist as these molecules aggregate together. [24] Whilst the large non-polar and aromatic groups facilitate Van der Waals and π- π stacking interactions, other interactions have also been suggested

to play a part in this aggregation, including interactions with MPs.[27] This poses even more difficulties in oil refinement, as aggregation can cause viscosity changes, physical adsorption to solid surfaces, or even precipitation of the asphaltenes out of the oil. Such processes can have a major effect on oil transportation since they can cause blockages. These complications, alongside direct catalyst poisoning, mean MPs can affect all areas of oil refinement. [25-27]

For all these reasons, the reliable identification of MPs in oil samples is of key importance. One of the primary techniques used to identify MPs in petroleum samples is UV/Vis absorption spectroscopy. Porphyrins have very distinct absorption profiles, characterized by two features, an intense "Soret" or B band at around 400 nm, and a series of weaker Q bands around 550 nm. [28] A solution phase spectra of tetraphenyl porphyrin (TPP) is shown below in Figure 1.2. This exhibits the characteristic Soret and Q bands present in a porphyrin spectrum.

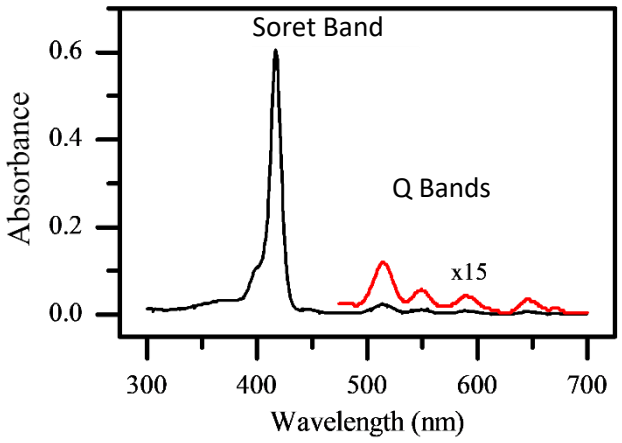

Figure 1.2: *The UV/Vis absorption spectrum of tetraphenyl porphyrin (1x10^5 M concentration) in DCM:MeOH (80%:20%) recorded on Shimadzu spectrophotometer. The absorption profile is typical of a porphyrin, with an intense Soret band around 400 nm, and single or multiple Q bands between 500-700 nm.*

The absorption coefficient at the Soret band for TPP is around 5 x 10^5 M^{-1} cm^{-1}. This is in line with other organic porphyrin molecules which all have absorption coefficients of roughly 10^5 M^{-1} cm^{-1}, as recorded by Rimington. [29] Metaloporphyrins share this incredibly strong absorption with tetraphenylporphine iron(III) chloride (FeTPPCl) having an absorption coefficient of 2.14 x 10^5 in the Soret region.[30] The origins of these transitions had been the subject of intense discussion [31] but it was Gouterman's four orbital model that eventually provided the widely used interpretation of the transitions. [32] This theory states that the absorptions are due to transitions between two HOMO and two LUMO orbitals (π to π* transitions), and that the metal centre and ring substitution can affect the relative energies of these transitions.

The two HOMOs are assigned as a_{1u} and a_{2u} symmetry orbitals, while the LUMOs are both of e_g symmetry. Two excited singlet states are formed when an electron is promoted, with an $a_{1u}e_g$ and an $a_{2u}e_g$ configuration respectively. [33] This is shown in figure 1.3 part 1 and b. Orbital mixing splits these two excited singlet states into a higher energy ^1E_u state, giving rise to the Soret band, and a lower energy ^1E_u state with considerably less oscillator strength, giving rise to the Q-bands. This is shown in figure 1.3 part c. The state mixing results in parallel and anti-parallel transition dipole moments, leading to the higher energy mixed state ($S_0 \rightarrow S_2$) transition being exceptionally strongly allowed, and the lower energy transition ($S_0 \rightarrow S_1$), only less strongly allowed. [33,34] The strongly allowed Soret (B) band typically has a molar absorption coefficient or around of 5 x 10^5 M^{-1} cm^{-1}, whereas the less strongly allowed Q bands are in the order of 3 x 10^5 M^{-1} cm^{-1} . [30]

Metal porphyrins have D_{4h} symmetry and their electronic excited states are E_u. There are equivalent dipole transitions in the x and y directions. In the un-metallated TPP, the x and y directions are no longer equivalent, as only 2 protons sit inside the porphin ring, giving D_{2h} symmetry. The increased symmetry of the metallated porphyrin makes more orbitals doubly degenerate, reducing the number of observed peaks in the Q band region.

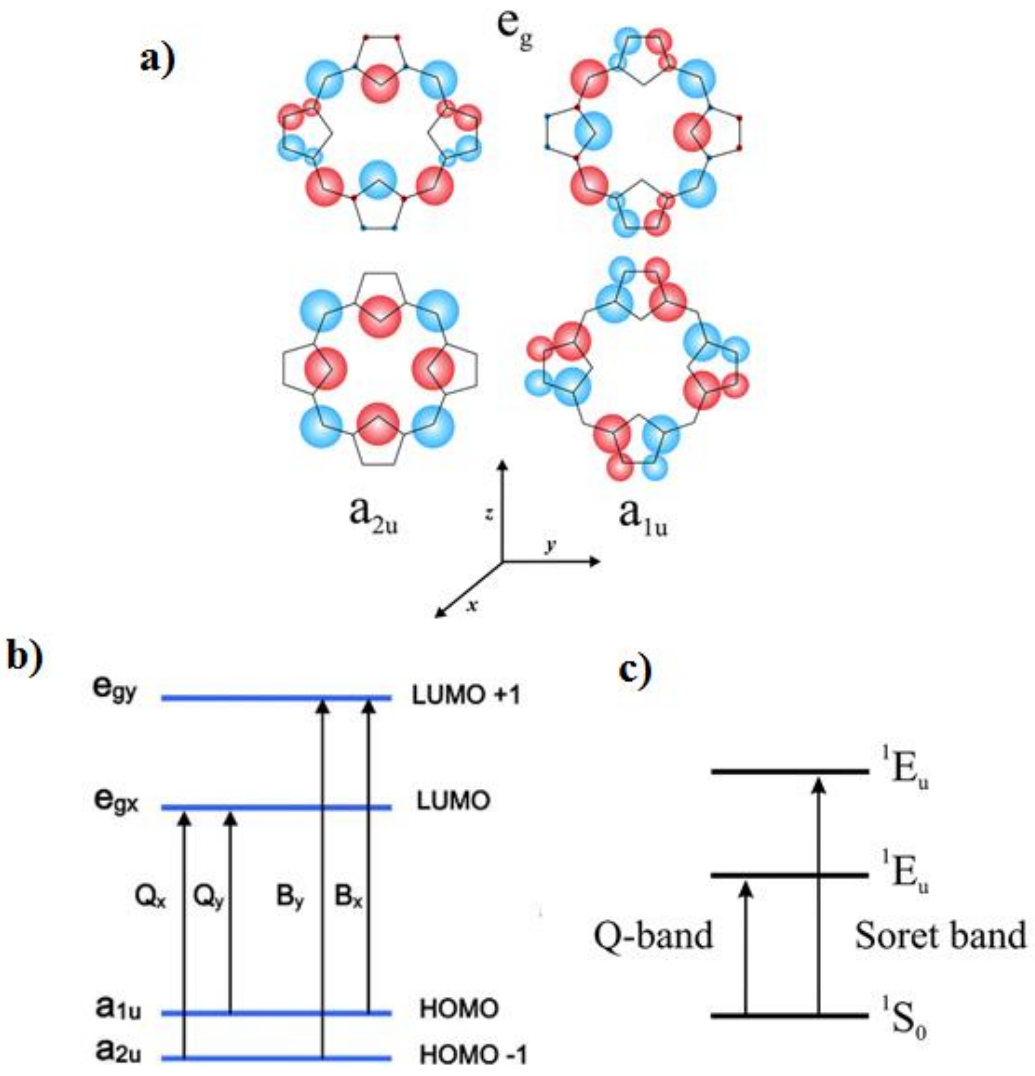

Figure 1.3. *a) The HOMO and LUMO orbitals of the porphyrin ring, showing the a_{1u}, a_{2u} and e_g symmetries. b) The energy levels of the transition showing the HOMO and LUMO orbitals and dipole transitions. And c) A simplified energy level diagram showing the ($S_0 \rightarrow S_2$) Soret and the ($S_0 \rightarrow S_1$) Q band transitions. Adapted from reference 25 and 33.*

Vibronic bands in the porphyrins have also been studied by numerous groups, including by Gouterman et al. [35] This previous work has used the simplified porphyrin model of a 16-membered cyclic polyene with 18 electrons which gives an oversimplified approach to gain a complete understanding of the vibronic levels. More recently, Minaev et al. have performed DFT calculations on the Q bands in order to predict with more accuracy the vibronic transitions by considering all vibrational movements and their interaction with electrons.[36] Figure 1.4 shows a fluorescence and fluorescence-excitation (absorption) spectrum of H_2TPP in the Q band region cooled to 77K.

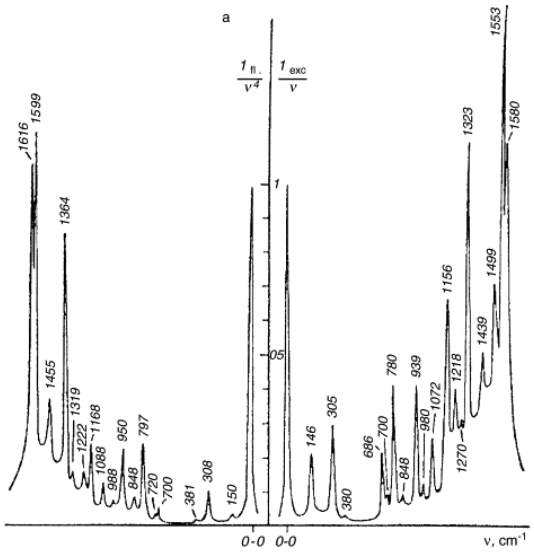

Figure 1.4: *Fluorescence and fluorescence-excitation (absorption) spectrum of H_2TPP in hexane at 77 K showing the large number of vibrational bands associated with a Q band transition. Figure taken from reference 37*

Given the well-known and distinctive absorption profile of porphyrins, it should in principle be easy to identify MPs in oil. UV/Vis spectroscopy of oil however brings many complications. Q band position and intensity is strongly affected by the metal ion and type of substituents on the porphyrin ring. For this reason, the Soret band is easier to study.[17,20] Although less affected by porphyrin substitution than the Q bands, the Soret band is found to be both weaker and broader than expected for the

given concentrations of MPs in oil.[20] Background noise caused by other species absorbing in the Soret region also complicates the bulk spectra. Much work has therefore been focused on investigating the immediate environment that surrounds the porphyrin and how it effects the porphyrin's absorption characteristics.

Using multiple different instrumental methods such as X-Ray diffraction and gel permeation chromatography, Dickie et al. analysed the heavy asphaltic fractions of oil. The proposed macrostructure showed the MPs were buried within the stacked aromatic sheets of polycyclic asphaltene compounds.[38] MPs are thought to be trapped inside these aggregations thus reducing the observed absorption coefficients. Stoyanov et al. subsequently proposed that the Soret band may be modified due to covalent attachment of larger aromatics and other asphaltene molecules, either through axial coordination of the metal centre or fusion (annellation) to aromatic rings on the porphyrin π-system. [39] Further work using Density Functional Theory calculations (DFT) has been performed on this axial coordination [40]

Because the local environment of is such importance to these systems, and it can have a large effect on the electronic structure, it is highly desirable to study the molecules in an isolated state, away from solvent perturbations. Gas-phase studies provide an ideal way to explore these intrinsic electronic properties and provide an unambiguous measurement of the MP absorption spectrum. Such studies also have the advantage of providing results that can be directly comparable to theoretical studies such DFT and Time Dependent-DFT (TD-DFT) methods, which have become common due to their relatively low computational cost. [41-43]

Some early examples of gas phase research on porphyrins are by Jortner et al. in the 1980's. The florescence spectra of TPP and ZnTPP were recorded following supersonic expansion to form vibrationally cold isolated gas phase porphyrin molecules. The fluorescence spectra of TPP and ZnTPP were recorded. [44] This was then extended to investigate porphyrins complexing with small molecules in the gas phase. Again, using supersonic expansion techniques, zinc octaethyl porphyrin was taken into the gas phase in helium gas seeded with either benzene, methanol, water, acetonitrile or pyridine. Complexes with all these species were reported, and laser induced florescence spectra were recorded. A red-shift was observed in these spectra relative to the uncomplexed species and attributed to stabilisation of the S_1 state by the complexing species. The stronger the molecules interaction with the porphyrin, the larger the red shift, and hence S_1 stabilisation. This can be seen by benzene, which interacts via Van der Waals interactions inducing a much smaller red shift compared to pyridine, where its lone pair forms a much stronger bond to the porphyrin. [45]

Mass spectrometry has been used over recent years to transfer MPs from solution into the gas phase. It has also been coupled with other spectroscopic techniques for analysing porphyrins and MPs in the gas phase. The first electrospray mass spectrometry of MPs was performed by Van Berkel et al. in 1993. [46] Ni and VO^{2+} centred porphyrins were studied because of their relevance to petroporphyrins. They detected free porphyrin as a $[M+H]^+$ peak and MPs $M^{\cdot+}$ radical cation in the mass spectra. Collison Induced Dissociation (CID) studies were used to investigate the fragmentation pathways. Similar work was carried out by Limbach et al., who used (Electrospray Ionisation) ESI to study MP mixtures. [47] More detailed CID experiments

on MP have been performed by Bohme et al. These studies focus on tetraphenyl iron and manganese porphyrins. [48] More recently Ion Mobility MS has been used in analysing petroporphyrins, as a method of quickly and reliably separating complex mixtures of many structurally similar porphyrins [49]

Much of the motivation to study porphyrin molecules comes from their prevalence in nature, especially their diverse number of roles in biological systems. By combining mass spectrometry with other analytical techniques allows for more insight to be gained about the species.

Some of the first examples of this combination was performed by J. M. Beames and A. J. Hudson. Building on the previous work by Jortner et al. this uses supersonic expansion techniques coupled with pulsed laser desorption to bring the porphyrin molecules into the gas phase. The resultant molecular beam produced is intersected with a UV laser pulse at 266 nm, and the ion signal is detected using a Time of Flight Mass Spectrometer (TOF-MS). An additional laser in the visible region is introduced allowing excited electronic states to be analysed via resonant-enhanced multiphoton ionization (REMPI). [50]

More recently, gas phase action spectroscopy, a technique that measures photodepletion and photofragmentation of gas-phase species with respect to wavelength has been performed on porphyrin systems. *Nielsen et al.*, have investigated the heme and chlorophyll systems. As the porphyrin ring in these species sits inside a protein pocket, its local environment is not equivalent to a bulk solvent. This potentially makes the gas phase spectroscopy more akin to a true biological system than a solution phase experiment.

Nielsen et al.'s studies of Fe(III)heme show an intense Soret feature at 381 nm and three Q bands between 450-600 nm. The dominant photodissociation pathway is by a loss of a CH_2COOH group, with the double loss of this group being a minor fragment. Time dependent studies were also performed using pump probe techniques. Two exponential functions were required to model the decay, and this was interpreted as being due to two competing pathways. One in which an Internal Conversion (IC) to the ground state forms vibrationally hot ions that relax, and the second where an Intersystem Crossing (ISC) moves it to a lower lying triplet state, followed by a second ISC back to the ground state. [51,52] Figure 1.5 is a Jablonski diagram that summarises this process.

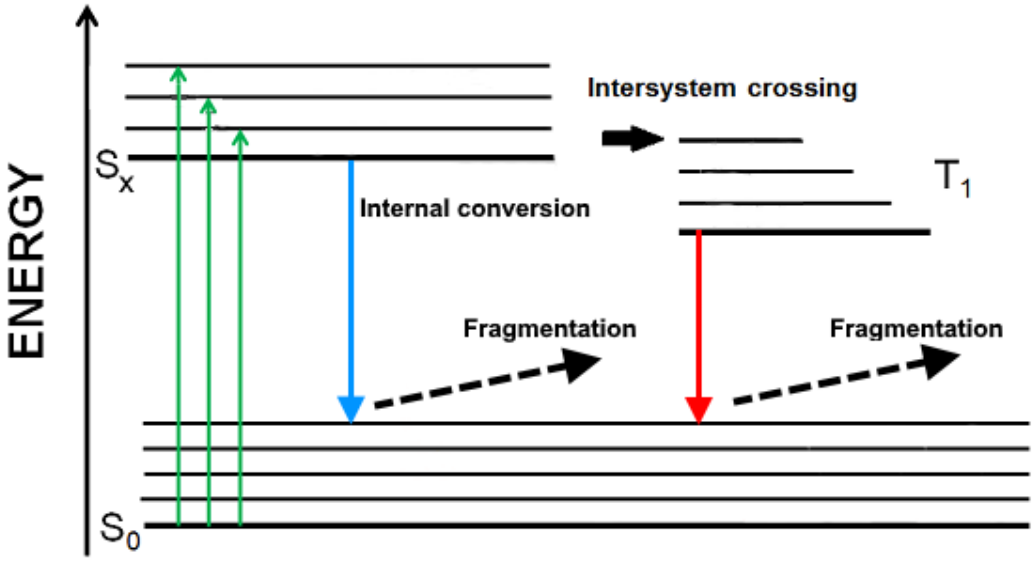

Figure 1.5: *Jablonski diagram representing the two competing pathways of Fe(III)heme. The first pathway follows the blue arrow which represents an IC to a vibrationally excited ground state where fragmentation occurs, and the second pathway follows an ISC to a triplet state, followed by a second ISC to a vibrationally excited ground state where fragmentation occurs.*

Dugourd et al. have also used action spectroscopy with an electrospray source to investigate the whole protein ferri-cytochrome c in the gas phase. The iron

containing heme group is the major spectroscopic feature, and a Soret band is clearly resolved with a maximum around 410 nm. This is red shifted by 30 nm from the free $[Fe(III)\text{-}Heme]^+$ which is in agreement with work by Nielsen that the protein environment is red shifting in nature. [53,54]

Whilst mass spectrometry is a very convenient method to manipulate and analyse different species in the gas phase, it does require the species to be charged. This still allows many different applications, but often it is desirable for the neutral form of the molecule to be studied. One way to get around this is by adding a charged group or "tag" to the molecule of interest, but ensuring it is sufficient distance away from the chromophore to not affect the absorption profile. The presence of a charged group allows the species to be ionised and manipulated in the MS, but maintains the chromophore in a neutral state. One such example of this with porphyrins are the experiments performed by Nielsen where a charged tag was to attached chlorophyll to explore its photodepletion spectra. Three different tags, including tetramethylammonium (TMA) were used to be sure the chromophore wasn't being affected. On photoexcitation, the $[Chlorophyll.TMA]^+$ complex dissociated, leaving the neutral chlorophyll and charged TMA. As neutral molecules cannot be detected, the yield of charged tag was measured relative to wavelength. For chlorophyll A and B this technique showed the Soret bands in vacuo were blue shifted compared to solvent or inside photosynthetic proteins, showing these environments are red shifting in nature. Charge tagging has also been applied to explore chlorophyll A dimers and axially ligated chlorophyll A and B. In each case the positions of the bands change. Computational techniques are used alongside many of these experimental methods to aid in interpterion of results .[54-56]

The combination of computational and gas phase techniques has also been recently used to study anionic porphyrins using photoelectron spectroscopy. [57] Electron affinity and vertical detachment energies were recorded by Bowen at al. for iron, manganese and nickel tetraphenyl porphyrins, with good agreement to previously performed theoretical studies. [58,59] Kappes et al. have also recorded PES on Mn and Cu centred meso-tetra(4-sulfonatophenyl)porphyrin species, as monomers, dimers and trimers. Using these spectra alongside DFT calculations the structures of the dimers and trimers were resolved. Specifically the manganese species were found to bind through sulfonic acid−manganese bonds, whereas the Cu porphyrins bound to each other via a sodium counter ion from the salt. [60]

1.2 Summary and Thesis Aims

As outlined above, the gas-phase study of MPs is an expanding field, but this has been largely focused to date on biologically relevant species such as heme and chlorophyll. Limited work has been performed on how microsolvation will affect the absorption profile of porphyrins and particularly for geologically relevant MPs. As very few of these petroporphyrins have been studied in the gas-phase, the main aims of this work is to study the absorption and fragmentation of gas-phase MPs, and to begin to understand how the clustering of small aromatic molecules affects these species in the gas-phase.

The specific aims of the research are:

- Obtain electronic spectra of isolated gas-phase metalloporphyrins without condensed-phase complications. By surveying a range of MPs, including

porphyrins with different metal centres, we can obtain a series of benchmarks of the key gas phase MP spectra

- Produce gas-phase cluster aggregates of metalloporphyrins coordinated to aromatic molecules through electrospray of mixed solutions. Electronic spectra of gaseous mass-selected cluster aggregates will reveal the extent to which axial coordination modifies the absorption bands.

In this thesis the gas phase photodepletion and photo fragmentation spectra of TPP, Hemin, FeTPPCl, VOTPP, NiTPP, VOOEP and NiOEP are reported. In addition to this, work has been carried out to form gas-phase clusters of Fe and VO centred porphyrins with pyridine and quinoline.

Chapter 2: Background Theory and Experimental methods

2.1 Background Theory

2.1.1 Electrospray Ionization

As with many of the mass spectrometry based studies described in the introduction, electrospray ionization (ESI) is used in these experiments to bring the species being studied into the gas-phase.

ESI is an ionization method that was first performed by Yamashita and Fenn and 1983.[61] A solution is pushed through a needle held at a potential of a few kV relative to a capillary. A cone of ionized liquid (known as a Taylor Cone) forms at the end of the needle as a result of this potential and emits charged droplets containing the analyte and solvent. As these droplets move towards the capillary, the solvent evaporates, aided by drying gas and the elevated temperatures of the capillary. This solvent evaporation leaves the droplets with more charge per unit volume, eventually leading to a point where the charge repulsion is greater than the surface tension of the droplet. This point is known as the Raleigh limit, and causes the droplet to undergo fission, where it splits into multiple smaller droplets. This process then repeats itself multiple times.[62] The precise mechanism of the final ion formation is still debated but is thought to be one of two methods; the Ion Evaporation Model (IEM); or the Charge Residue Model (CRM). [63] CRM simply suggests that repeated fission and evaporation cycles continue until induvial gas phase ions are left and was

proposed by Dole et al.[64] The IEM model suggests that at a critical radius, the charge in a droplet is enough to induce a field desorption, whereby individual gas phase ions can evaporate from the surface of the droplet, and was proposed later by Iribarne and Thomson in 1975. [65] The process may also be a combination of these two pathways, but the result is charged, gas phase molecules, that can be manipulated inside a mass spectrometer. The ESI process in summarized below in Figure 2.1.

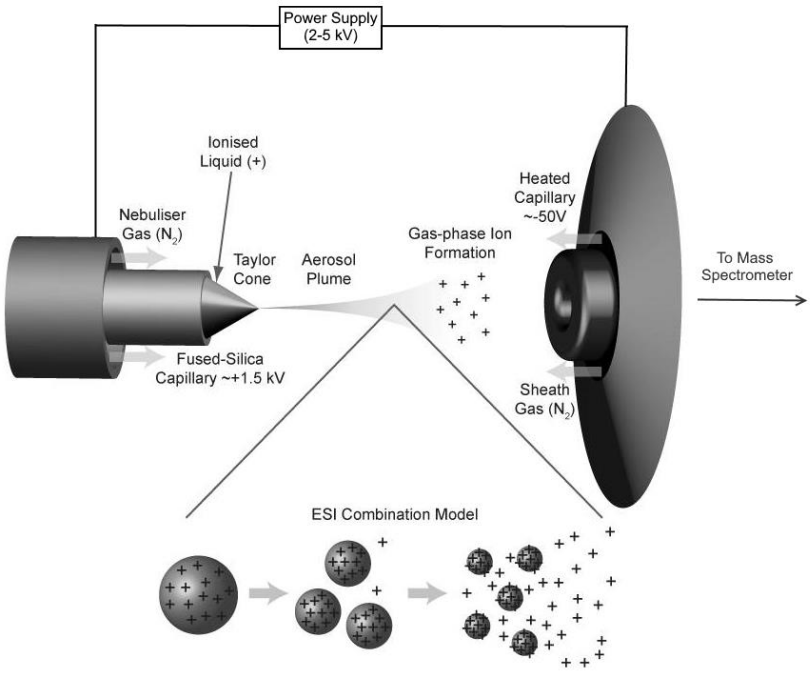

Figure 2.1: *Schematic diagram of an ESI source. As solution is forced through the charged needle, a Taylor cone is formed, ejecting charged droplets. These charged droplets are attracted towards the oppositely charged capillary. As they travel, solvent is evaporated and the excess charge on the droplets surface causes fission to occur. This process repeats, and eventually forms mono-charged ions. ESI Figure adapted from reference 62.*

ESI is a "soft" ionisation technique since, compared to methods such as Electron Ionisation (EI) as there is very little fragmentation caused by the ionization process. This allows large species to be brought into the gas phase as their molecular ions.

Intermolecular interactions that are present in solution can also be transferred intact into the gas phase, which is crucial for allowing the study of species that are clustered together. ESI is a highly versatile technique. So long as a solution can be produced of the desired sample, using a suitable solvent, it will generally be ionised by ESI. The technique can be used in positive or negative mode, depending on how the species will favourably ionize, allowing both cations and anions to be produced and studied.

There are however solvent considerations that must be considered when using ESI. In positive mode, where positive species are required, there must be a source of protons for the species to bind to and form the respective $[M+H]^+$ cation. Aprotic solvents will not work in isolation, eg dichloromethane (DCM) alone is insufficient and requires and addition of a more protic solvent eg MeOH. For samples that are more difficult to protonate, organic acids such as acetic or trifluoracetic acid can be used. For these reasons, mixed solvent systems are often used. Salt adducts are also a common issue, with $[M+Na]^+$ and $[M+K]^+$ peaks appearing in almost all positive mode spectra, as these ions are very hard to fully eradicate.

2.1.2 Quadrupole Ion Trap

A Quadrupole Ion Trap (QIT) is an ion trapping and mass selecting tool used in some types of mass spectrometers. The QIT itself consists of a central cavity surrounded by a ring electrode and two end caps above and below, as shown in Figure 2.2 .[67]

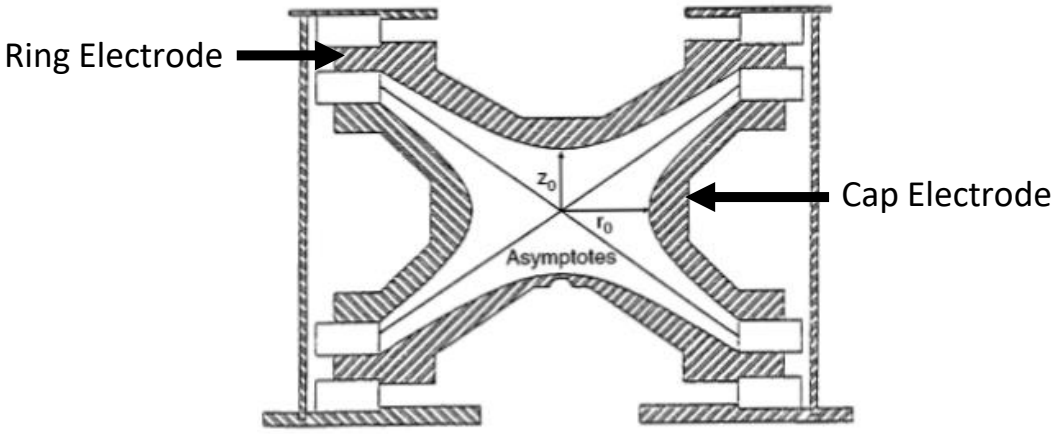

Figure 2.2: *Schematic cross-sectional diagram of a Quadrupole ion trap. Ions are trapped inside the central cavity until selectively ejected. Figure taken from reference 67.*

Ions are controlled inside this trap by applying an RF potential to the ring electrode. This makes the ions inside the trap oscillate at their own "secular" frequency. Mass ejection is carried out by applying a voltage to the end caps at the secular frequency of the desired ion. This makes the ion's oscillations unstable and allows them to be ejected. The trap is buffered by He gas which cools and collisionally dampens the ions, which repel each other.[67] The trapping ability of the QIT is utilised in the photodissociation experiments as the packets of ions trapped inside the QIT can be irradiated by overlapping a laser pulse with them. The time these ions spend inside the QIT is called the isolation window and this is controlled using software. This is expanded in more detail in section 2.1.4

2.1.3 Collision induced dissociation (CID)

Ion control using resonant excitation is used in the low energy fragmentation technique Collision Induced Dissociation (CID). By resonantly exciting, but not expelling an ion, the number of collisions it undergoes with the He buffer gas will increase. The energies of these collisions can then be increased by increasing the resonant voltage. Each collision raises the internal energy of the ion and if the energy is high enough it will lead to fragmentation.[68] In typical analytical mass spectrometry this is useful as it provides fragment information, and hence primary structure information, that may not be present when soft ionization techniques such as ESI are used. Here, it is useful as it can be used to explore the low-energy ground-state dissociation pathways of a species. These are equivalent to the decay pathways followed by an ion following thermal excitation. It is useful to compare the thermal ground state fragments to the photofragments, to establish whether thermal dissociation of the ground state occurred after photoexcitation.

2.1.4 Gas-Phase Photodissociation Experiments

Gas phase absorption spectra provide an insight into a molecule's behaviour away from any perturbating effects of solvent. Measuring the absorption in the gas phase however comes with some complications. Unlike solution phase techniques where the change in intensity of the input light can be directly measured, the number of trapped ions in the gas phase (usually $10^3 – 10^6$) is insufficient to observe any change in the laser intensity. Instead, absorption is measured indirectly by following the "action" of the ions following photoexcitation. This can be through the depletion of

parent ions, or production of fragments. Figure 2.3 shows the mass spectra produced when the laser is off and on. The formation of numerous photo induced fragments is apparent.

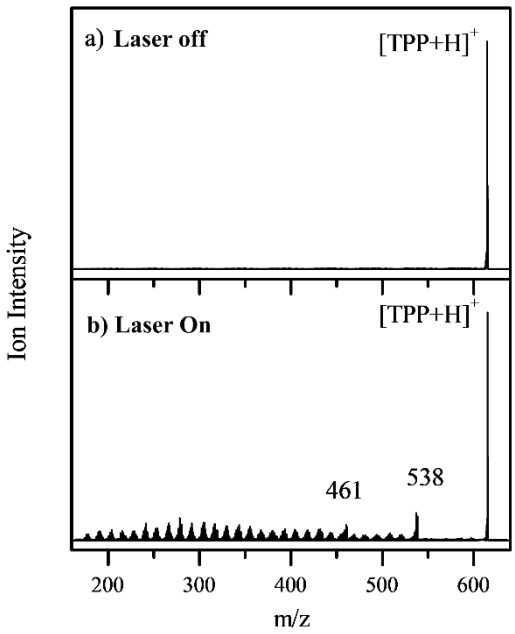

Figure 2.3 *Total ion mass spectra showing the isolated [TPP.H]+ when the laser is a) off and b) on. Fragments are present as two major peaks at m/z=538 and 461, as well as multiple low intensity fragments.*

When interacted with the laser pulse the mass selected ion will be electronically excited. From this point its behaviour will be determined by its photophysical properties. As the ion is in the gas phase there is no vibrational relaxation route available with solvent interactions, so the excess vibrational energy could cause direct fragmentation from the excited state. Rapid IC or ISC may also occur taking the ion back to a vibrationally excited ground state or triplet state respectively, where again fragmentation could take place. In this case the fragment ions would be same as those produced in CID experiments. An ion may be able lose some energy via an

internal energy wasting process and reform the ground state ion without fragmentation. This is summarised in the Jablonski diagram in Figure 2.4.

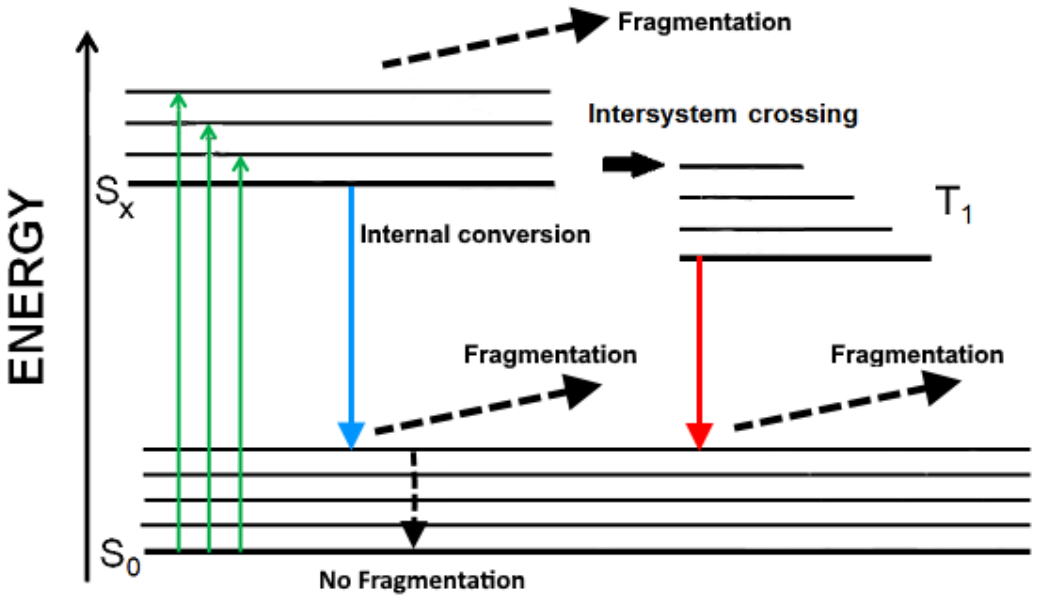

Figure 2.4 *Jablonski diagram showing the potential routes of fragmentation or relaxation following excitation.*

In this experimental setup radiative emission (fluorescence and phosphorescence) cannot be detected and hence would show as no fragmentation.

Photodepletion (and photofragment production) can be calculated in numerous different ways, using the intensity of the signal from the mass spectrometer when the laser is on (I) and when the laser is off (I_0). These calculations can also be corrected for laser power, and its wavelength. [69-73] Depletion can be measured in a logarithmic (equation 2.1) or linear way (equation 2.2), although both produce internally comparable results. The logarithmic relationship however is adapted from

the Beer-Lambert law and recognises that absorption is exponentially related to the decay in laser intensity, therefore is used predominantly.

$$D = \mathrm{Ln}\frac{I_0}{I} \quad \text{(Eq 2.1)}$$

$$D = 1 - \frac{I}{I_0} \quad \text{(Eq 2.2)}$$

The depletion (D) is modified to approximate the gas-phase absorption cross section (ε), otherwise known as the total photodepletion (PD), by correcting for the irradiation variables, laser power (P) and number of laser shots (t). An additional correction is often made to the laser power by multiplying through by the photon energy (hν) or dividing through by the wavelength (λ) in order to represent the photon number density.

$$PD = \frac{D}{P\,t} \quad \text{(Eq 2.3)}$$

$$PD = \frac{D}{P\,t}\,h\nu = \frac{D}{P\,t\,\lambda} \quad \text{(Eq 2.4)}$$

Photodepletion methods assume that each photon that is absorbed leads to fragmentation with a uniform probability across the scanned region. In the UV region of 400 – 100 nm (3.1 – 12.4 eV) the photon energies are sufficiently large that absorption will lead to fragmentation with a near unit probability in many biologically important organic and inorganic ions. At lower photon energies in the visible part of the part of the spectrum multi-photon effects must be considered. Photofragment (PF) production is usually calculated using the fragment ion intensity (I_F) and the same corrections applied to the photodepletion calculations.

$$PF = \frac{I_F}{P\,t\,\lambda} \quad \text{(Eq 2.5)}$$

$$PF = \frac{I_F}{I_0} \times \frac{1}{P\,t\,\lambda} \qquad \text{(Eq 2.6)}$$

Gaseous spectroscopy of polyatomic ions was first carried out by Dunbar in 1971 on methyl chloride cations. An ion cyclotron resonance (ICR) mass spectrometer was used to trap ions in a known location and irradiate them with monochromatic light in the UV region. By measuring production of the CH_3^+ ion across each wavelength, Dunbar compiled a gaseous absorption spectrum.[74,75] This apparatus was subsequently used to study other cationic systems in the gas phase.[76-79] This was followed by work on anionic species by Brauman, who observed electron detachment and fragmentation. [80] These initial action spectroscopy experiments used an EI source on a mass spectrometer to generate gas-phase ions, causing considerable amounts of fragmentation before irradiation could take place. This limited the species that could be studied. Modern action spectroscopy setups utilize the softer ionization techniques such as ESI. These enable much larger systems to be studied, including spectroscopy of isolated, weakly bound clusters and complex biomolecules. These modern setups are typically a) modified commercially available MS instruments, or b) fully custom-built setups. Commercial mass spectrometers benefit from typically being highly reliable and low maintenance systems. Data acquisition and processing can also benefit from professionally made software provided by the manufacturer. They are however, unlike custom machines, typically much harder to modify and tailor to the experimental conditions desired. This makes continual updating of an experiment harder.

Several research groups currently use commercially available mass spectrometers that have been adapted for spectroscopy measurements. The first such instrument

came from the Weinkauf group, whose experiment used a modified electrospray ionization quadrupole ion trap mass spectrometer (ESI-QIT-MS, Esquire 3000, Bruker Daltonik).[81] Here a liquid N_2-cooled QIT is used to trap ions and which are internally cooled through collisions with the liquid N_2-cooled He buffer gas. Laser light for absorption experiments was produced by a tuneable dye laser which was aligned through the exit aperture of the QIT, and absorption by ionic species was calculated from the production of photofragments as a function of wavelength. Protonated tryptophan $[Trp\text{-}H]^+$ was studied using this apparatus, resolving the $S_0 - S_1$ band between 283 – 286 nm. [81]

In the current project, a commercially available AmaZon 6000, Bruker Daltonik Mass Spectrometer (ESI-QIT-MS), has been used. The ion trapping ability of the QIT is used to store ions, allowing laser light to be introduced to the stored gas phase ions and induce photodissociation. Modifications to allow for laser interaction with the ion packet were performed by Bruker and are reviewed in the next section.

2.16 OPO

A neodymium-doped yttrium aluminium garnet (Nd:YAG, $Nd:Y_3Al_5O_{12}$) laser (Surelite, Continuum) was used in the mass spectrometry experiments to pump an optical parametric oscillator (OPO) laser (Horizon, Continuum) at 10 Hz. An optical parametric process is a three-photon interaction, where a single photon (the pump) is split into two lower energy photons, the higher energy photon is called the signal and the lower energy photon is called the idler. For this process to occur, the energy and momentum of the initial photon must be conserved in the two photons that are produced. This OPO allowed a total wavelength range of 192 – 2750 nm to be

accessed, although in these experiments measurements were only taken between 290 and 700 nm. The Nd:YAG laser has a fundamental wavelength of 1064 nm and frequency doubling and mixing is used to generate the second and third harmonics which are at 532 and 355 nm respectively. An outcome of how the OPO operates is that two separate outputs are present on the OPO, one which outputs the UV light at 192 – 400 nm and a second for the visible and IR light at 400 – 2750 nm. When scanning across this changeover it is necessary to manually adjust the positions of three of the internal optics inside the OPO as well as software control.

A consequence of the output being in a different position is that a different optical route is required for the UV and visible/IR photons. This introduces an additional challenge as the beam shape and position is not identical when the OPO is switched over, and the Soret band of typical porphyrins is in this region. A schematic diagram of the OPO is shown in Figure 2.5, showing the two separate outputs.

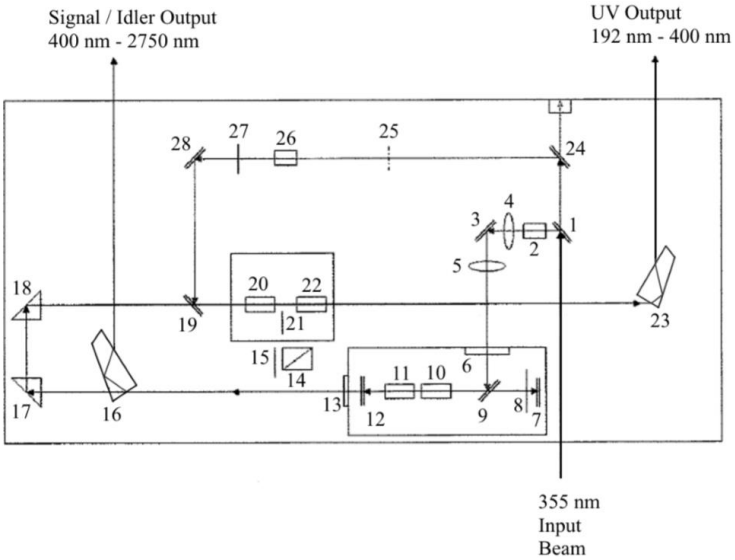

Figure 2.5: *Horizon OPO optical layout showing 2 different exit ports. Individual optics are not described. This image has been adapted from and more information can be found in the Horizon OPO manual (reference 82).*

2.17 DFT

A small amount of computational chemistry has been used in this thesis to support and explain the experimental photodepletion spectra. All of these quantum chemical calculations have been calculated using density functional theory (DFT). These calculations provide an "optimised" lowest energy structure of the calculated molecule found in the gas phase. These structures are then used to simulate electronic excitation spectra using time-dependent density functional theory (TDDFT). This was used to aid in the interpretation of the experimental spectra to assign certain structures. Gaussian 09 was used for all calculations,[85] employing the B3LYP functional with the 6-311G* basis set, as previously used by Stoyanov et al.[39,40]

2.2 Experimental Methods

UV laser photo-depletion and fragmentation experiments were conducted by using the following modifications to the AmaZon ion-trap mass spectrometer: Two laser windows (UV-fused silica) have been installed in the top flange of the vacuum chamber to provide entrance and exit ports for the laser beam. Two 2 mm holes have been drilled through the ring electrodes, thus allowing the laser beam a path through the centre of the trap. The RF circuit was retuned following the drilling of the holes so that the performance of the mass spectrometer is unaffected by these modifications. The helium pressure within the modified trap is maintained at 5×10^{-6} mbar. A pair of mirrors is situated beneath the ion trap to allow the laser beam to exit the mass spectrometer after passing through the ion trap to assist laser

alignment. A 200 mm UV fused silica focusing lens (focal length 30 cm) is used to reduce the beam diameter to ~2 mm when entering the mass spectrometer and is placed such that the focal point occurs within the mass spectrometer. These modifications are summarized in Figure 2.6.

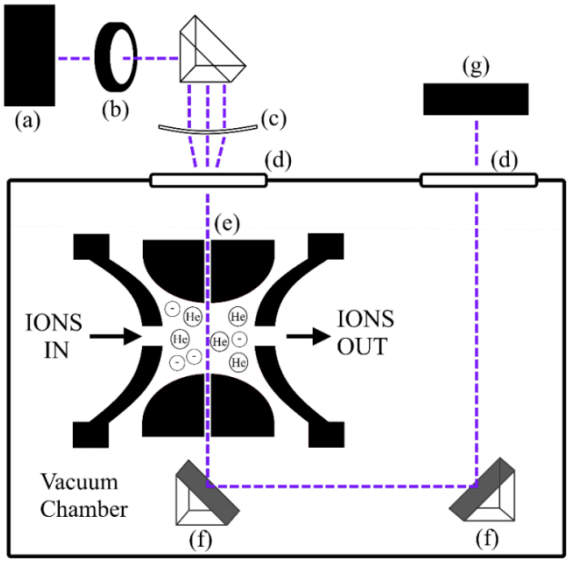

Figure 2.6: *Schematic diagram of the experimental apparatus and the modifications to the Bruker amaZon mass used in these studies, Where (a) is an Nd:YAG pumped OPO (Panther Ex) tuneable laser; (b) is an optical shutter (c) is a 200 mm focal length UV-fused silica lens; (d) is a pair of flange mounted uncoated UV-fused silica windows; (e) is a 2 mm hole drilled through the ring electrode of the ion trap to allow the passage of laser light;*

The ion signal was optimized using the automatic tuning capabilities, with typical selected settings of nebulizing gas pressure of 10.0 psi, injection rate of 250 µL/hr, drying flow rate of 8.0 L min^{-1}, capillary temperature of 100 ^{o}C, and ion isolation time of 5 -100 ms. Low-energy collision induced dissociation (CID) was performed on isolated ions by applying an excitation AC voltage to the end caps of the trap to induce collisions of the trapped ions with the He buffer gas. Further detail of these

experiments are explained elsewhere. [77,78] Fragment ions with m/z less than 50 are not detectable in the instrument since low masses fall outside of the mass window of the trap.

The UV laser light was produced from an Nd:YAG laser (Continuum Surelite) pumped OPO (Panther) across 215-399 nm. The energy of the photons was monitored using an adjustable power meter and was adjusted to 1 mJ for all wavelengths by adjusting prism positions using the inbuilt software. All instrument parameters and laser experiments were controlled via the AmaZon software. A typical spectral scan sequence consists of: clear ion trap, accumulate ions in trap (typically 20 – 100 ms), mass selected ion isolation within the trap, fragmentation and mass scan. The MS_n functionality of the mass spectrometer is used to store ions for a variable time period (typically 100 – 500 ms) during the fragmentation window in which they are exposed to the laser. The fragmentation stage is commonly used to study the collision induced dissociation of gaseous ions, but for a laser scan, the CID amplitude is set at 0 V. A beam shutter (Model SH05, Thorlabs Inc) is used to control the laser beam transmission into the mass spectrometer, and is triggered by the mass spectrometer such that the ion trap is only irradiated during the fragmentation phase of the mass spectrum acquisition.

The photodepletion intensity (PD) and the photofragment production (PF) were calculated using equations 2.7 and 2.8 and are presented as a function of the photon energy, expressed in wavelength.

$$\text{Photodepletion Intensity} = \frac{\text{Ln}\left(\frac{\text{Int}_{\text{OFF}}}{\text{Int}_{\text{ON}}}\right)}{\lambda \times P} \qquad \text{(Eq 2.7)}$$

$$\text{Photofragmentation Production} = \frac{\left(\frac{Int_{Frag}}{Int_{OFF}}\right)}{\lambda \times P} \quad \text{(Eq 2.8)}$$

A alternative way to calculate PD, based on the numerical depletion method is also used, it is detailed in equation 2.9:

$$\text{Numerical depletion} = \frac{\left(\frac{Int_{Frag}}{Int_{OFF}}\right)}{\lambda \times P} \quad \text{(Eq 2.9)}$$

Where Int_{ON} and Int_{OFF} are the peak intensities of the ions with laser on and the laser off. Int_{Frag} is the fragment intensity with the laser on, λ is the excitation wavelength (nm) and P is the laser pulse energy (mJ).

For CID experiments, ion intensity is averaged over a thirty second acquisition window. For all UV laser photo-depletion and fragmentation experiments, a one-minute acquisition window was generally used. All experiments were run under one-photon conditions, by ensuring that the photodepletion intensity increases linearly with laser power at several points across the scanned spectral region. For all the gas-phase action spectroscopy experiments, 100 ml solutions of the porphyrin were made up in 80:20 DCM:MeOH. This mixture was necessary to aid protonation in the electrospray as DCM was not an adequate source of protons.

All solution phase UV absorption spectra were recorded on a Shimadzu UV-1800 spectrophotometer. Samples were run between $1x10^{-3}$ and $1x10^{-6}$ M concentration. A 0.5 nm step size was used between 220-800 nm.

TPP and FeTPPCl were purchased from Sigma-Aldrich (95% purity), VOTPP was purchased from Santa Cruz Biotechnology (90 % purity). All porphyrins were used without further purification.

Chapter 3: Tetraphenyl Porphyrin

3.1 Introduction

As discussed in the introduction, studying molecules in the gas phase can provide a wealth of information, typically from a "ground-up" approach. Of particular interest, is how the distinctive absorption profile of porphyrins is "lost" in oil samples. Absorption appears much weaker than is expected, making identification more difficult. Using action spectroscopy on trapped ions, the fundamental absorption and fragmentation properties of isolated porphyrin/ MP molecules can be explored. Then, clusters of porphyrins and relevant molecules found in petroleum can be made. By building up this external environment and measuring absorption cross sections as a function of wavelength, the effect of complexation on the porphyrin spectrum can be directly measured. As previous gas phase studies had been performed on un-metallated (TPP), [86,87] it was selected as an initial test species to assess the viability of the ESI-QIT photodissociation experiments.

3.2 TPP Results and Discussion

TPP is a synthetic porphyrin, although metal containing TPP complexes are known geoporphyrins. In its neutral state, it is highly symmetric with a D_{2h} symmetry and has a characteristic solution phase absorption profile with an intense Soret band (λ_{max} = 415 nm) and four Q bands (λ_{max} = 514, 549, 589, 646 nm) This absorption profile is shown in Figure 3.1.

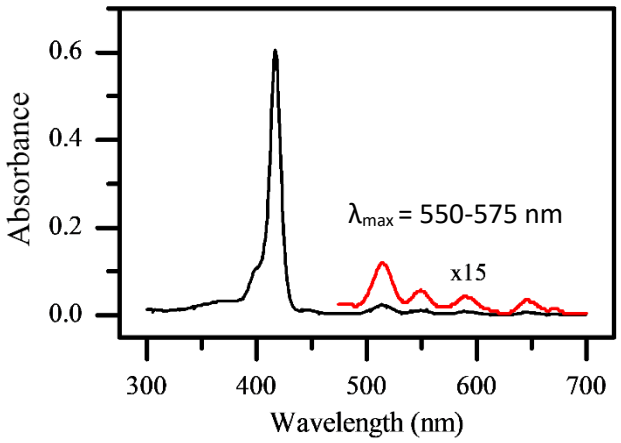

Figure 3.1 : *Solution phase UV spectra of TPP recorded in DCM:MeOH (80%:20%) at 1x10^{-5} M concentration.*

On protonation this high symmetry (D_{2h}) is lost, and the resulting mono protonated TPP ($TPP.H^{+}$) is formed. Figure 3.2 shows the solution phase spectum of a protonated TPP sample, where the Soret band has redshifted and the four Q bands have now become two bands.

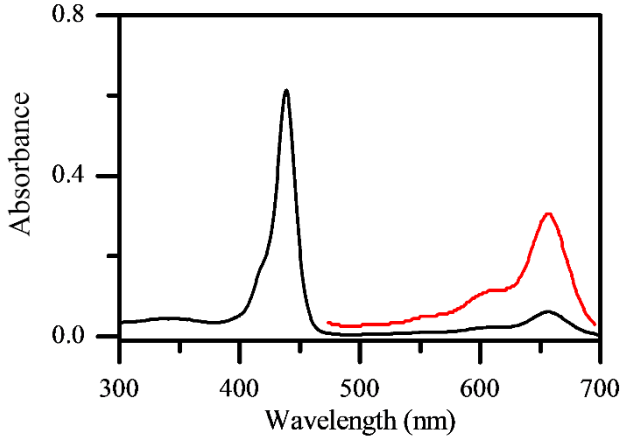

Figure 3.2 : *Solution phase UV spectra of TPP recorded in DCM:MeOH (80%:20%) at 1x10^{-5} M concentration at pH 3.*

The Soret band appears asymmetrical, with a shoulder on the blue side. This could be due to aggrgation of the porphyrin molecules [28] or a weakly resolved vibronic band. Given the low concentrations used ($1x10^{-5}$ M) arrigration is less favored and vibronic strcutre is known in this region for porphyrins, so this is most likely the cause for this. [44]

In both spectra the Soret band is TPP was electrosprayed from a solution of DCM:MeOH (80%:20%). This solvent system was used to maximise solubility and to provide a sutable proton source for the electrospray to work. The most intense peak seen in the mass spectrum was at m/z =615, correlating to a singly protonated $[TPP.H]^+$ species. This is as expected from Van Berkel et al., [46] where all free base porphyrins studied were detected as $[M+H]^+$. A photodepletion spectrum of this mass selected species was recorded across the 300 - 650 nm region and is shown below in Figure 3.3. A broad absorption with λ_{max} =420 nm is the major feature which would correlate well to the protonated Soret band position observed in solution. This is notably blue shifted by 19 nm from the protonated solution spectra. A weaker and broader feature is observed between 520 and 600 nm, with two overlapping bands at λ_{max} =550 nm and λ_{max} =575nm which would correspond to the Q bands. In the protonated solution these are present at 610 and 655 nm, a blue shift of 60 nm and 80 nm respectively.

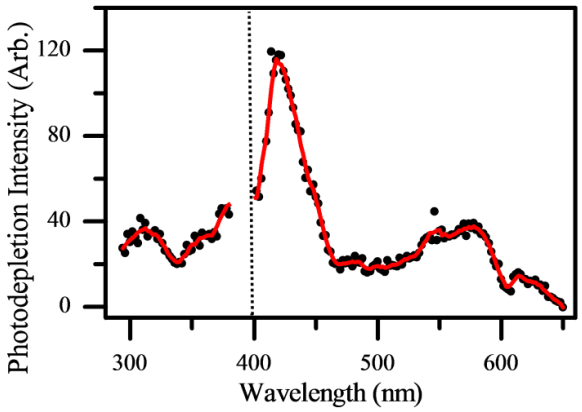

Figure 3.3: *Photodepletion spectra calculated as difference in parent ion intensity between irradiated and non-irradiated $[TPP.H]^+$, calibrated for laser power. 1 nm scan below 400nm and 5nm scan above 400nm. The solid line represents a three-point adjacent average of the data. The dashed line represents the wavelength switch over on the OPO.*

Although complicated by the wavelength switch over on the OPO, the Soret band appears asymmetrical on the higher energy side, as with the solution phase spectrum. Vibrational structure is seldom resolved in these experiments as the ions are electrosprayed at high temperatures and ion trap is at room temperature. This is therefore likely to be the partially resolved vibronic structure that was seen in the solution phase spectrum.

Even et al. have performed fluorescence excitation experiments on vibrationally cold H_2TPP molecules and shown these vibrational levels. [44] Figure 3.4 shows these vibronic transitions in a cold isolated molecule of H_2TPP. The "tailing" effect towards the higher energies is of note for later discussion.

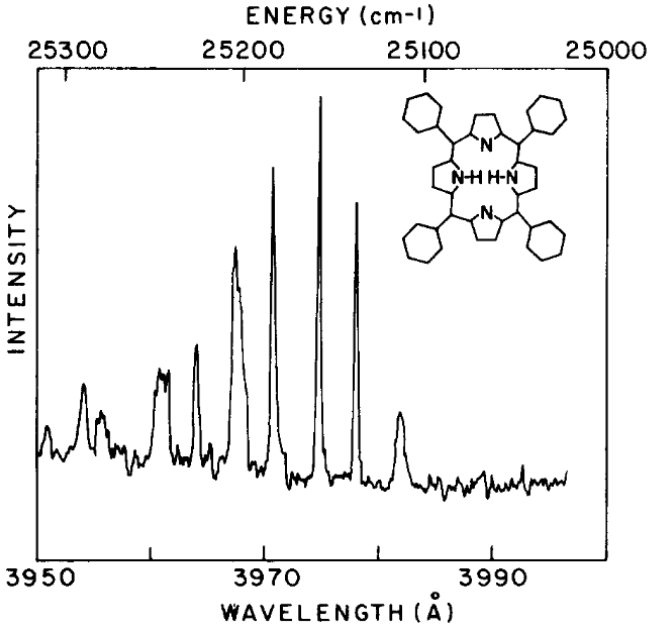

Figure 3.4 *Absorption spectrum of H_2TPP showing the vibronic transitions of the Soret band. Image taken from reference 35*

The ground state fragmentation properties of $[TPP.H]^+$ can be explored using the low-energy CID functionality of the quadrupole ion trap. Under CID conditions a single major fragment is observed at m/z =538. This represents a loss of m/z =77 and can be rationalized as the loss of a neutral phenyl radical. The CID curves and presumed pathway are shown below in Figures 3.5 and 3.6.

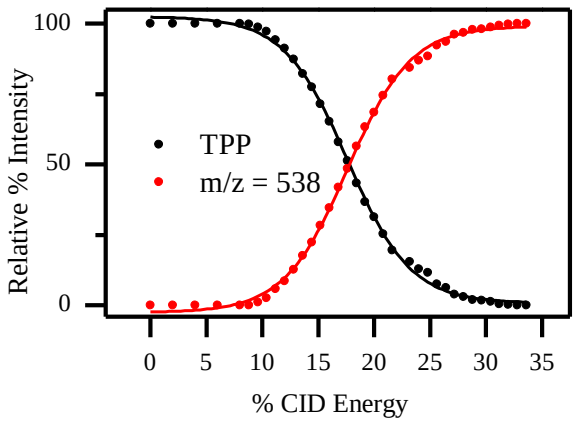

Figure 3.5: *CID curves showing relative intensity of parent and fragment ions against % CID energy for* $[TPP.H]^+$

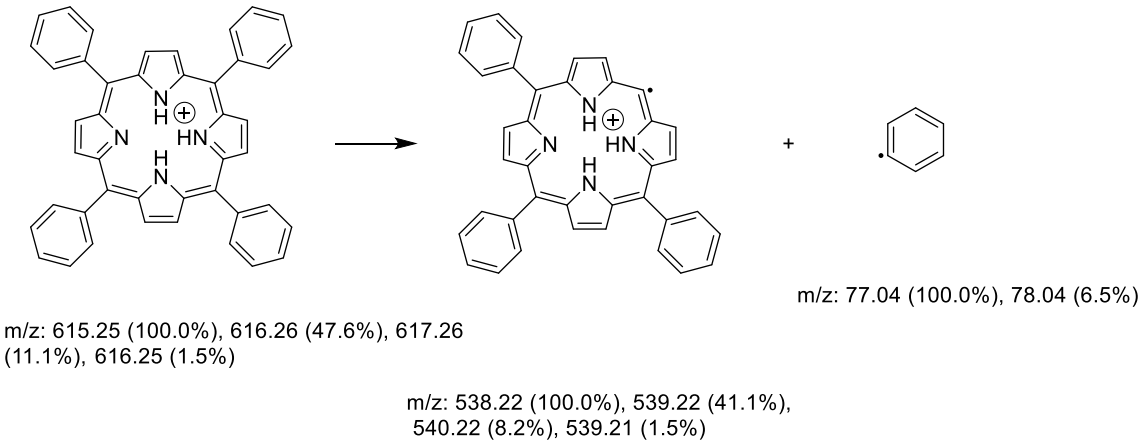

Figure 3.6 : *Presumed fragmentation pathway of* $[TPP.H]^+$ *under CID conditions to produce a fragment at m/z = 538 and an undetected phenyl radical.*

Loss of a phenyl radical is an expected pathway and is common for metallated $[TPP.H]^+$ molecules as shown by Gozet et al. [48]

Under photochemical conditions two major fragment ions were observed, at m/z =538 and 461. These were assigned as loss of one and two phenyl radicals respectively. The photofragment spectra of the two species are shown in Figure 3.7.

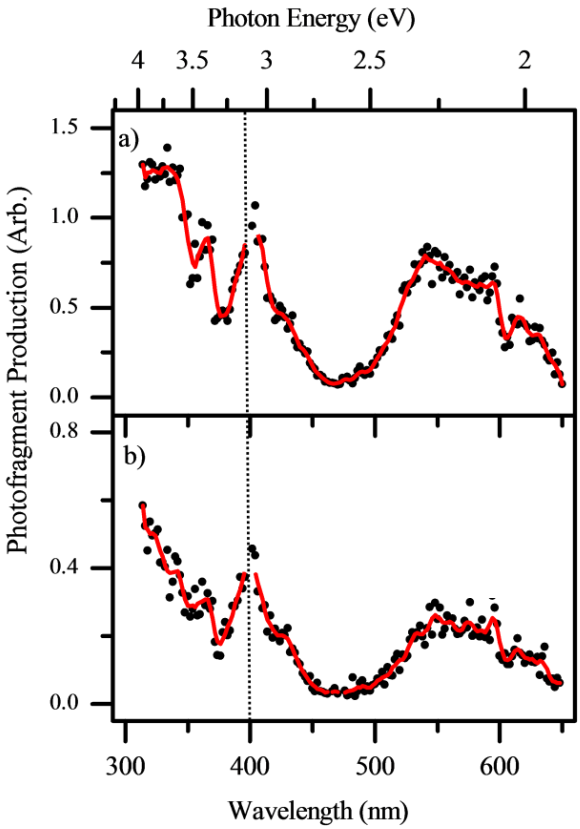

Figure 3.7 : *a) Photofragmentation spectra calculated as difference in parent ion intensity between irradiated and non-irradiated $[TPP.H]^+$ calibrated for laser power for a) fragment m/z =538 and b) m/z = 461. The solid line represents a three-point adjacent average of the data. The dashed line represents the wavelength switch over on the OPO.*

The overall absorption cross section is very similar for both species, suggesting both fragmentation pathways occur by the same mechanism. Absorption in the Q band region is enhanced in the photofragment spectra compared to the photodepletion spectra.

As well as these two major photofragments at m/z =538 and m/z =461 multiple lower intensity fragments are also produced upon irradiation, this is clearly seen in the whole ion mass spectrum shown in Figure 3.8.

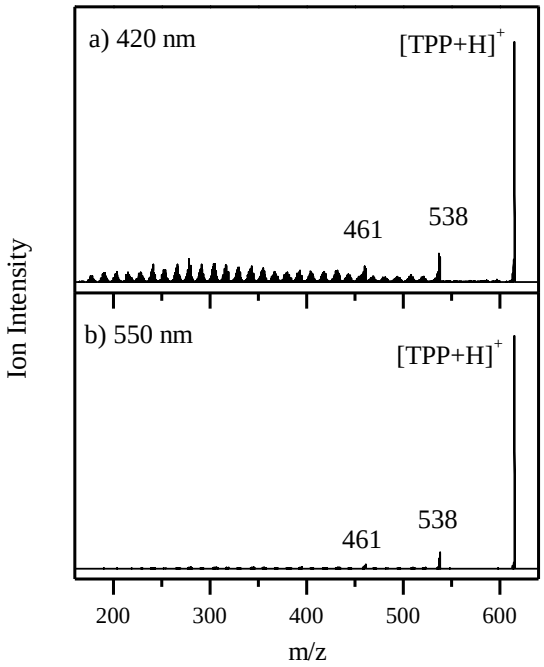

Figure 3.8 : *MS showing the photofragment production when irradiated with radiation at a) 420 nm and b) 550 nm. Whilst the two major photofragments occur in both spectrum, the multiple, low intensity fragments only occur In the Soret region.*

The formation of these low intensity fragments is much higher in the Soret band region.

Both CID and laser studies show the two major fragments at m/z =538 and 461. This is in agreement with Giacomozzi et al., who performed high energy CID experiments with energies between 50–110 eV on TPP. [86] These ground state collisions are far in excess of the photon energies used in the PD studies and should be more comparable to the photo induced dissociation. The results of Giacomozzi et al. are shown below in Figure 3.9:

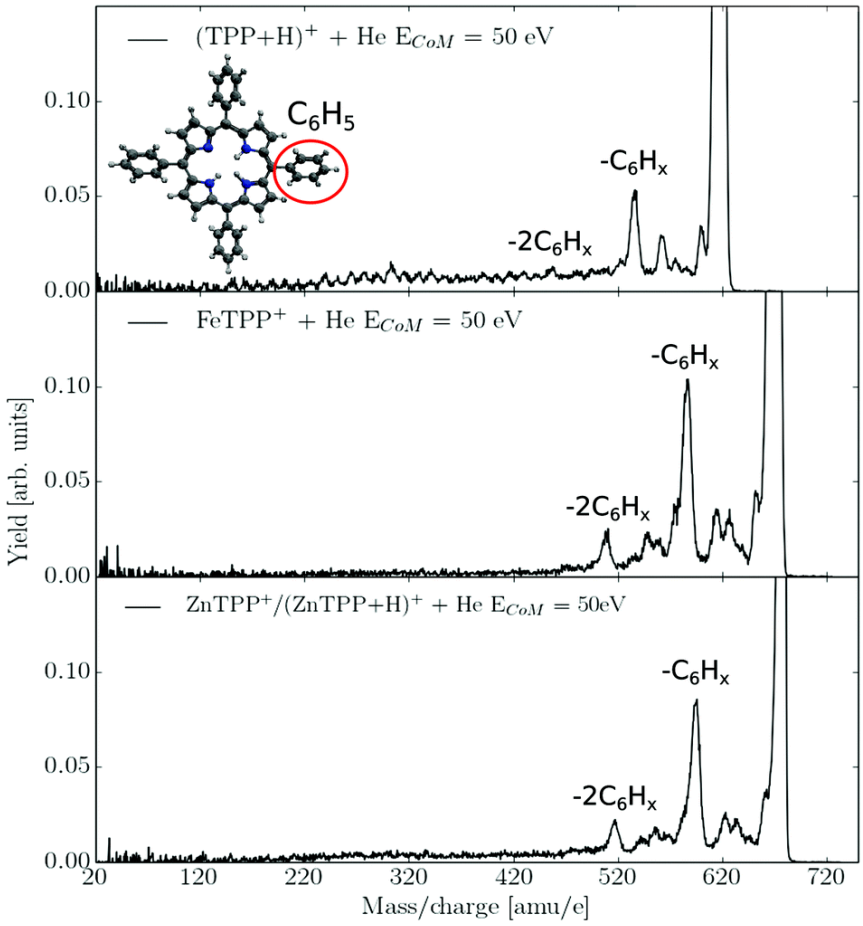

Figure 3.9 : *50 eV CID MS results from Giacomozzi et al. recorded for $[TPP.H]^+$ FeTPP and ZnTPP. Major fragment loss for $[TPP.H]^+$ are attributed to loss of one or two C_6H_5 groups. Multiple low intensity peaks are also observed. Figure taken from reference 86.*

Similar high energy CID experiments on $[TPP.H]^+$ have also shown this multiple fragmentation pathway. For example, Nielsen et al. have also recorded dissociation spectra of at 50 eV. [87] Loss of one or two of the aromatic rings was the dominant fragmentation pathway, and multiple low intensity fragments were also observed. Further to this experiment, lifetime analysis experiments were performed by monitoring fragmentation when irradiated at 390 nm. This revealed two that

dissociation channels were occurring, with time constants of 81 μs and 1.7 ms respectively. The decay profile for this is shown in Figure 3.10.

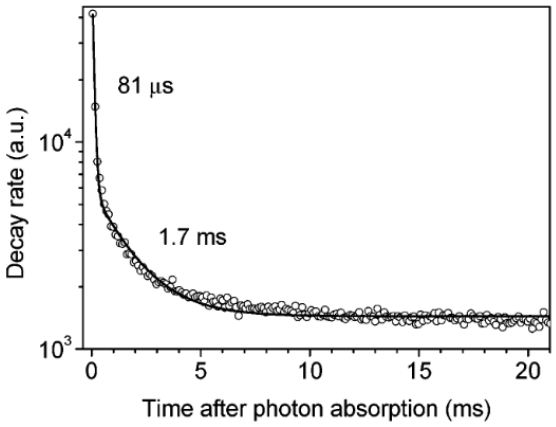

Figure 3.10: *Decay profile for TPP.H + showing the two resolved lifetimes of 81 μs and 1.7 ms.*

The presence of the two channels is explained by two competing dissociation routes, one of which is via the formation of a triplet state. Porphyrin triplet states are well known [88] and have been shown to form for the protonated $[TPP.H]^+$ species. [89] Populating this state increases the time before the system can relax into the vibrationally excited ground state, S_0^* and subsequently fragment. This would make it slower than the corresponding pathway which only contains singlet states. The two dissociation channels seen in this experiment may be the same as the two apparent channels seen in the $[TPP.H]^+$ photodissociation experiments. The singlet state pathway would most likely correspond to the major fragments seen at m/z =538 and 461. The triplet pathway would then produce the multiple lower intensity fragments over a longer time period. Figure 3.7 shows that in the Soret band region, the multiple low intensity fragments are produced in far greater amounts than in the Q band region, suggesting this triplet decay process is happening more at this point.

DFT calculations were performed using the B3LYP functional and the 6-31+G* basis set to determine the ground state geometry for neutral TPP. These calculations showed the neutral molecule's lowest-energy conformer exists with the central porphyrin ring in a planar arrangement and the four aromatic rings rotated out of the plane, which can be understood as a way to minimise steric hindrance. B3LYP / 6-311+G* was chosen as it had previously used for looking at TPP. Results are in line with other computational studies previously performed and bond distances are in good agreement with these earlier results e.g *Valiev* et al. gave a TPP structure with an internal H-H distance of *2.190* Å compared to 2.185 Å for the structure calculated in this work. [90]

To find the optimized protonated form, multiple $TPP.H^+$ structures were optimized, and the lowest energy conformer was selected. This conformer is shown below in Figure 3.11.

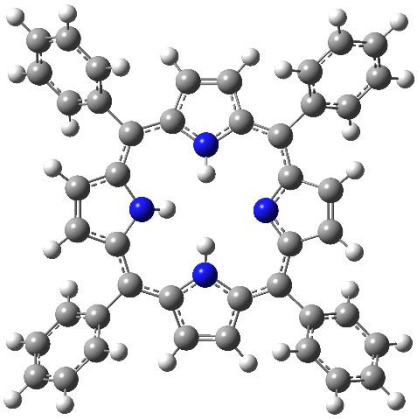

Figure 3.11: *Optimized ground state geometry of $[TPP.H]^+$ calculated at B3LYP/6-31G* level of theory*

This optimized geometry was used to calculate UV absorption spectra using TD-DFT methods. This can then be compared to the experimental spectra. By building a

collection of gas-phase MP spectra, TD-DFT methods can be benchmarked and used to evaluate excitations. The TD-DFT calculation, shown in Figure 3.12 predicts a Soret band at 410 nm and 2 excitations in the Q band region at 582 nm and 595 nm. These show a good correlation to the gas phase spectra recorded. The recorded λ_{max} for TPP experimentally was 420 nm and the for the TD-DFT, λ_{max} = 412. In the Q-band region a broad absorption is seen around 660 nm and the TD-DFT predicts two absorption at λ_{max} = 560 and 595 nm.

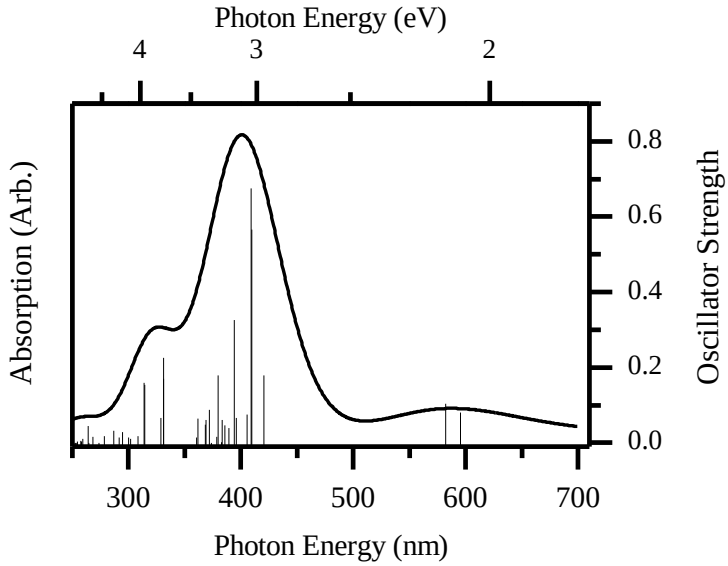

Figure 3.12: *UV/VIS spectra generated from a TD-DFT calculation of TPP at B3LYP/6-31G* level of theory at 50 states. The full line spectrum represents a convolution of the excitations with a Gaussian function (0.250 eV HWHM).*

These preliminary results show a good correlation between experimental and theoretical tests, but further work would be required to test different functionals and theory levels, especially for more demanding metal containing porphyrins.

3.3 Conclusions

TPP was readily electrosprayed and the $TPP.H^+$ species was well resolved in the mass spectrum. Despite the Soret band sitting on the OPO laser crossover point, the gas-phase absorption spectrum was recorded with Soret and Q band features being observed. Multiple, low intensity fragments were observed in the Soret region and these were assigned as fragments formed through a triplet state relaxation pathway, as previously recorded by Nielsen et al. Moving on from these results, the absorption characteristics of metallated porphyrins can now be explored.

Chapter 4: Metalloporphyrins

4.1 Introduction

Following from the work on TPP, metallated porphyrins were now chosen to be studied, as this is how they are typically found in biology and geologically. The first species chosen was hemin, which is a heme based porphyrin. Structurally it is the same as protoporphyrin IX, but contains a central Fe atom with a ligating Cl. This should provide a good metallated porphyrin test species as the Cl^- should dissociate allowing it to be readily electrosprayed. Nielsen et al. have studied the unmetallated protoporphyrin IX, which can be used to compare back too. [91]

4.2 Hemin

As shown in Figure 4.1, In the solution phase, hemin has a broad Soret peak centred at (λ_{max} = 398) but no strongly identifiable Q band features, although a slight deviation from the baseline is observed at around 500 nm.

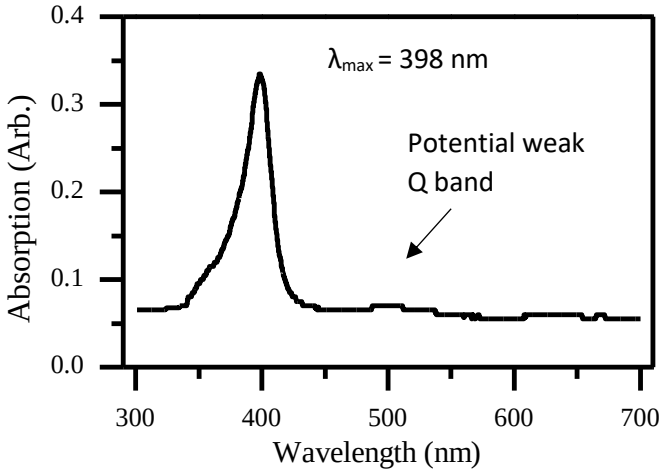

Figure 4.1: *Solution phase UV spectra of hemin recorded in MeCN:MeOH (80%:20%) at 1x10^{-5} M concentration*.

As with TPP, the band is asymmetric, indicating an unresolved vibronic structure. The photodepletion spectra, shown in Figure 4.2, showed a Soret band maxima at 370 nm, and a much weaker Q band feature at 500 nm. This correlates well to Nielson et al. who recorded maxima at 381 nm for the Soret band and Q band absorption in the region 450-600 nm. [91]

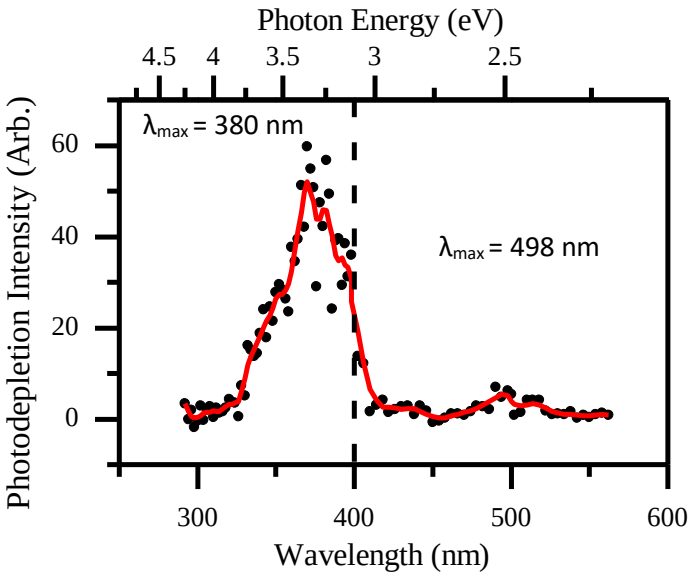

Figure 4.2: *Photodepletion spectra calculated as difference in parent ion intensity between irradiated and non-irradiated $[Hemin]^+$, calibrated for laser power. 2 nm scan below 400nm and 4nm scan above 400nm. The solid line represents a three point adjacent average of the data. The dashed line represents the wavelength switch over on the OPO.*

A blue shift of 18 nm is observed between the solution and the gas phase spectra. Nielsen previously studied hemin produced with a surrounding cage to prevent any perturbation of bands from solvent interaction which gave a maximum at 400 nm in solution, [52] very similar to the 398 nm maxima recorded in this solution spectra. Both would indicate that in solution the Soret transition is redshifted by approximately 20 nm.

Ground state fragmentation shows that 1 major fragment is produced at m/z = 557, corresponding to the loss of CH_2COOH. This fragmentation, and the expected pathway are shown below in Figures 4.3 and 4.4:

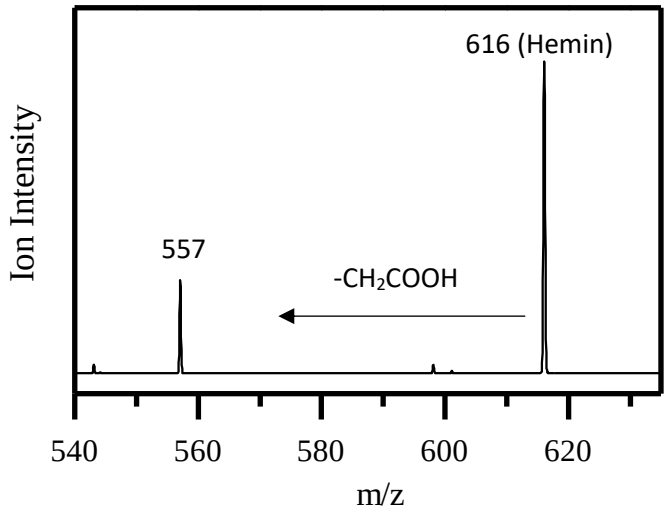

Figure 4.3: *Ground state fragmentation of hemin showing major fragment at m/z = 557. Fragmentation at 20% CID energy.*

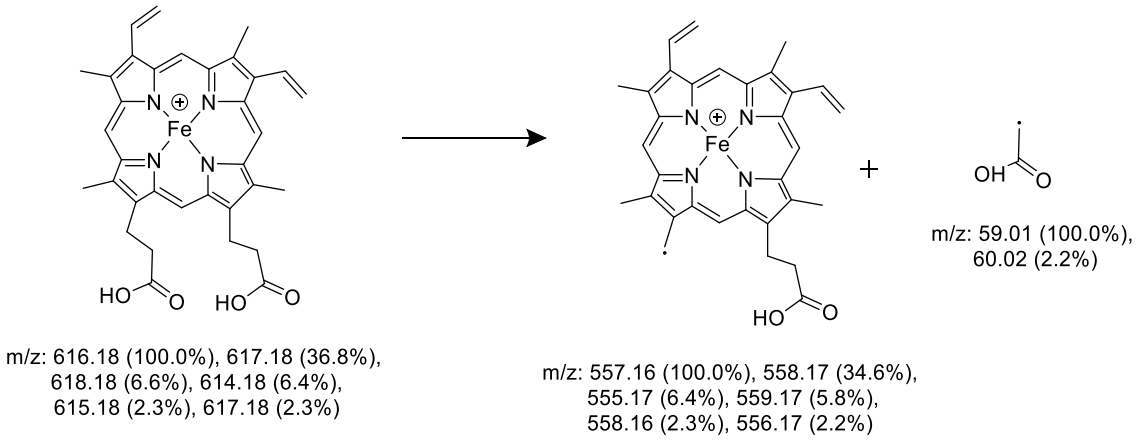

Figure 4.4: *Fragmentation pathway for the hemin cation, illustrating loss of a m/z = 59 unit*

Photochemically two fragments were produced, a major fragment at m/z =557 and a minor fragment at m/z = 498. These fragmentation pathways are the same as seen

in the ground state and correspond to the loss of one or two CH_2COOH groups. These photofragmentation spectra are shown in Figure 4.5.

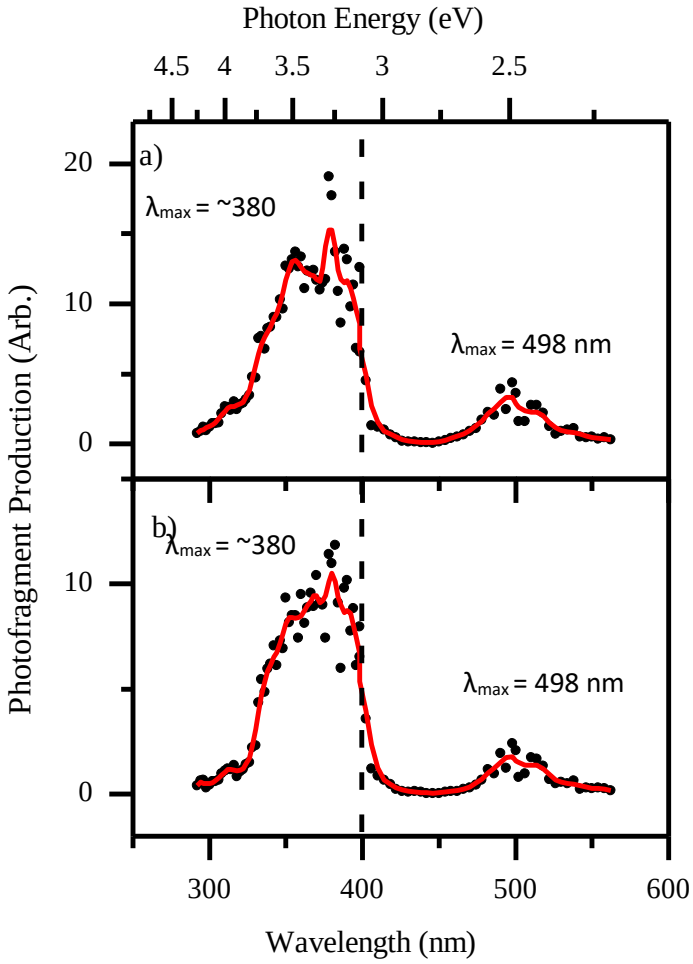

Figure 4.5: *Photofragmentation spectra calculated as difference in parent ion intensity between irradiated and non-irradiated $[Hemin]^+$ calibrated for laser power for a) fragment m/z =557 and b) m/z = 498. Readings were taken every 2 nm below 400 nm and every 4 nm above 400nm. The solid line represents a three-point adjacent average of the data. The dashed line represents the wavelength switch over on the OPO.*

As with the TPP, Nielsen et al. have also studied the fragmentation of protoporphyrin IX. [91] For this species they found three lifetime components, measuring 49 ± 20 μs, 0.36 ± 0.05 ms, and 6.5 ± 1 ms, when irradiated at 523 nm. The longer-lived decay pathway was again attributed to the decay proceeding via a triplet state ($S_1 \rightarrow T_1 \rightarrow S_0$).

The shortest-lived pathway was attributed to a singlet only pathway (IC from S_1 to S_0^*) followed by rapid dissociation. This pathway was assigned to the loss of the CH_2COOH groups. In the CID and PD experiments performed in this work, the loss of CH_2COOH groups were the major fragments and both absorption cross sections were the same. This indicates that the dissociation pathway was the same for each.

Unlike in TPP, hemin shows only a very small number of low intensity fragments associated with this triplet state decay during irradiation. The total ion MS of hemin irradiated at the Soret maxima is shown in Figure 4.6:

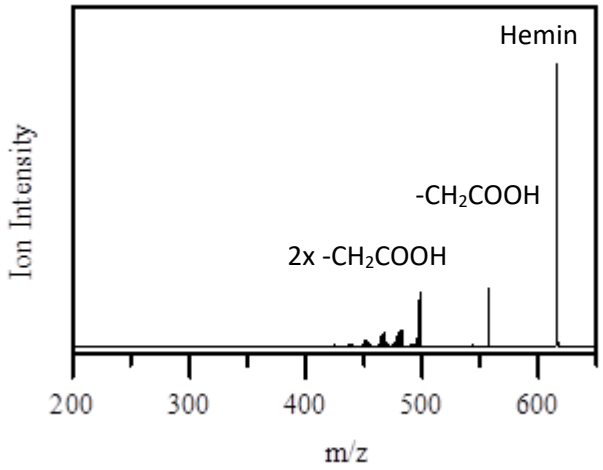

Figure 4.6: *Total ion MS of hemin when irradiated at the Soret band λ_{max} 380 nm. The 2 major fragments are visible as well as some low intensity fragmentation*

Comparing the total ion MS produced by hemin when irradiated at the Soret band to that of the respective TPP MS (Figure 3.7), it is clear that much fewer low intensity fragments are produced by hemin. This would suggest that the triplet decay pathway is much less pronounced when a metal ion is present, and the metallated porphyrins are more photostable.

4.3 FeTPPCl

As the TPP species electrosprayed well, and the Fe centred hemin also provided a strong ion signal upon electrospray, a range of metallated TPP species were selected to be investigated in the next stage of the project. The FeTPP was chosen as the first species to be investigated for comparison to the Fe centred hemin. To form FeTPP, the chlorinated salt Fe(III)TPPCl was used. The Cl^- coordinating ion dissociates in solution and allows the $FeTPP^+$ cation to be formed in positive mode electrospray.

A solution-phase spectrum of FeTPPCl was recorded in DCM:MeOH. The Soret band was observed at 396 nm. Only a single, symetric Q band was resolved, centred at 510 nm. This is shown in figure 4.7.

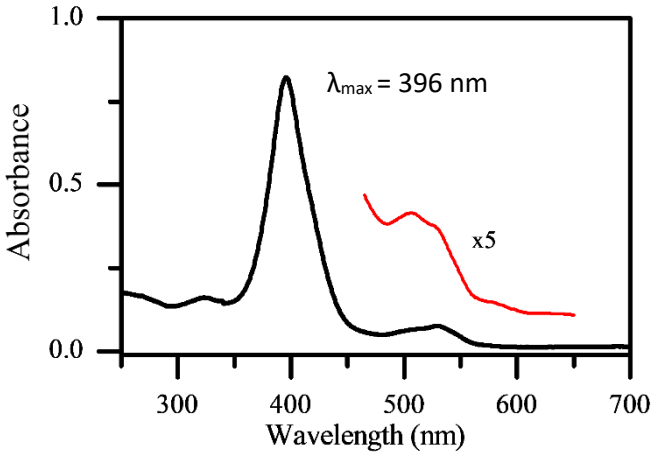

Figure 4.7: *Solution phase UV spectra of FeTPPCl recorded in* DCM:MeOH (80%:20%) at *$1x10^{-5}$ M concentration.*

When electrosprayed in positive mode the chloride ion of FeTPPCl dissociates, forming a positive $[FeTPP]^+$ ion with m/z = 668. Several other peaks were observed in this region and are assigned as isotope and protonation peaks. Figure 4.8 shows these peaks as detected in the total ion mass spectra.

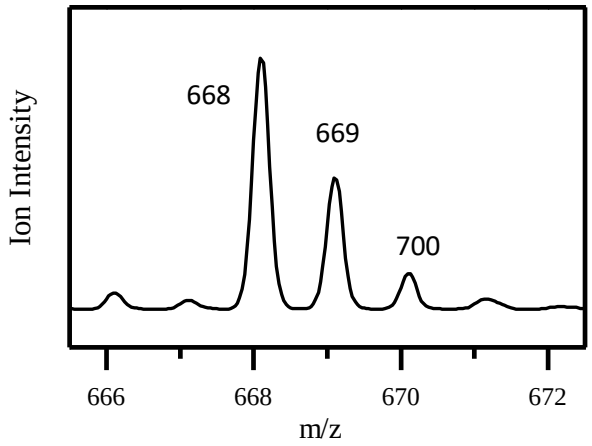

Figure 4.8: *MS showing the m/z = 668 $[FeTPP]^+$ ion, along with the m/z = 669 M +1 peak, and m/z=700 M+2 peak when the FeTPPCl species was ionised via ESI.*

Photodepletion and fragmentaton of $[FeTPP]^+$ was recorded across the 300 - 700 nm region. The photodepletion spectrum is shown below in Figure 3.16. The red line shows photodepletion at 1 mJ laser power. A broad absorption with λ_{max} = 382 is the Soret band, but no clearly identifiable features can be assigned to the Q bands. The blue line shows the Q band region scanned at 1.5 mJ laser power. This shows a broad absorption feature centred around 500 nm, in the expected region for a Q band in FeTPP. This spectral feature will be explored further in the photofragment spectra.

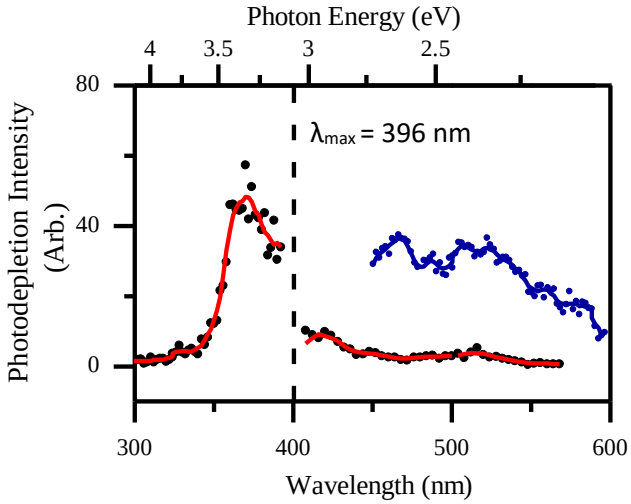

Figure 4.9: *Photodepletion spectra calculated as difference in parent ion intensity between irradiated and non-irradiated $[FeTPP]^+$, calibrated for laser power. 1 nm scan below 400nm and 5nm scan above 400nm. The solid line represents a three-point adjacent average of the data. The dashed line represents the wavelength switch over on the OPO. The red line shows photodepletion at 1 mJ laser power. The blue line shows the Q band region scanned at 1.5 mJ laser power.*

As with TPP, the major ground state fragment is the loss of a single phenyl radical at mass 77 Da. A second ground state fragment is also observed, corresponding the loss of a second phenyl radical.

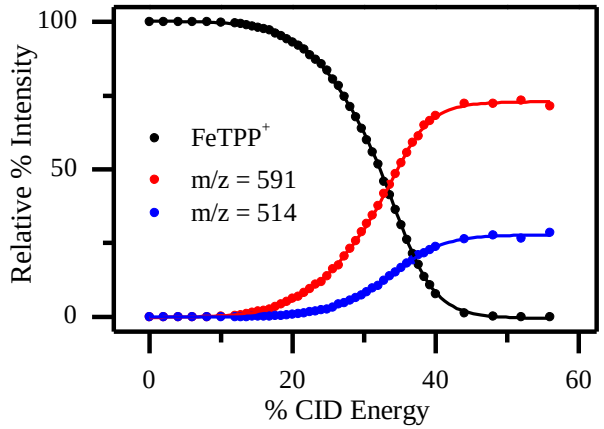

Figure 4.10: *CID curves showing relative intensity of parent and fragment ions against % CID energy for $[TPP.H]^+$*

These same two species were observed under photochemical conditions, with the loss of one phenyl radical ring (m/z = 591) being the major fragment. The photofragment spectra of this species is shown in Figure 3.18.

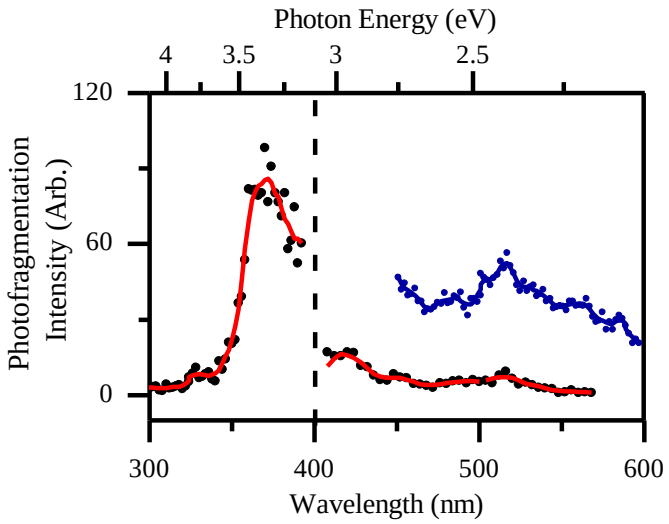

Figure 4.11: *Photofragmentation spectra calculated as difference in parent ion intensity between irradiated and non-irradiated [FeTPP]$^+$, calibrated for laser power for photofragment at m/z = 591. The solid line represents a three-point adjacent average of the data. The dashed line represents the wavelength switch over on the OPO. The red line shows photodepletion at 1 mJ laser power. The blue line shows the Q band region scanned at 1.5 mJ laser power.*

As with the PD spectra, pumping with 1 mJ laser power does not clearly resolve any Q band features, although a very weak feature is present at ~ 515 nm. On moving to a higher power this becomes much more pronounced, with a λ_{max} =516 nm. This enhancement of the Q band in the photofragment spectra is the same as is seen in TPP spectra. Loss of a phenyl radical was again the major fragment seen in the ground state and excited state. As seen with hemin however, there was a notable decrease in the number of low intensity fragments seen compared to the unmetallated TPP.

This again suggests that the central metal ion is stabilising the porphyrin ring with respect to the triplet decay pathway.

4.4 VOTPP

The second metallated porphyrin studied was vanadyl TPP (VOTPP), which is the neutral complex formed by the doubly deprotonated TPP^{2-} and the vanadyl ion (VO^{2+}) sitting in the centre. VOTPP is found as an inorganic contaminant in oil so is representative of a petroporphyrin. Its structure can be seen in Figure 4.12.

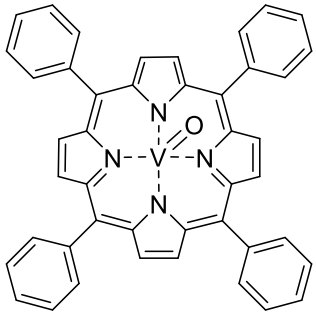

Figure 4.12: *The structure of VOTPP, a known geoporphyrin present in many oils.*

A solution phase spectrum of VOTPP was recorded in DCM:MeOH. The Soret band was observed at 423 nm, and a single Q band with at 547 nm.

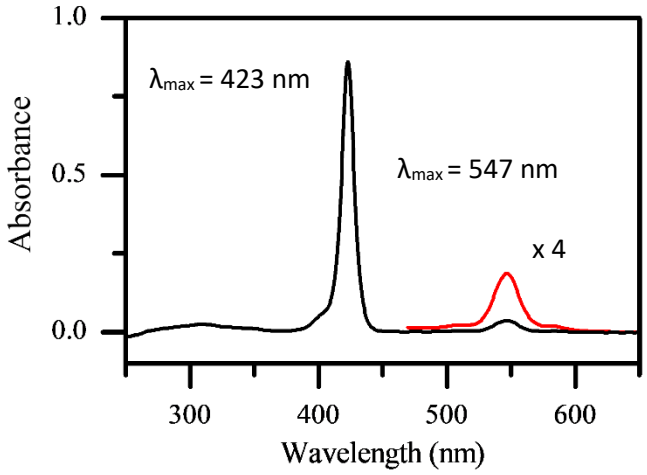

Figure 4.13: *Solution phase UV spectra of VOTPP recorded in DCM:MeOH (80%:20%) at* $1x10^{-5}$ *M concentration.*

When electrosprayed in positive mode, multiple peaks are present around the mass of VOTPP. Unlike $[FeTPP]^+$, vanadium only has one isotope, so the M+1 peak is attributed to the formation of a $[VOTPP.H]^+$ species forming in the electrospray. The most intense peak however corresponds to the formation of a $[VOTPP]^+$ species. This is in line with work on metalloporphyrins by Van Berkel et al. where the most intense species seen when MPs are electrosprayed is the oxidised $[Porphyrin]^+$ species. [46]

The photodepletion spectra shown in figure 4.14 resolves an intense Soret band with λ_{max} =392 nm, which is notably sharper than the $FeTPP^+$ species. This is in line with the solution phase spectra, where the half width full maximum (HWFM) of the VOTPP is much less than FeTPPCl. As with $[FeTPP]^+$ no Q band structure is resolved at 1 mJ laser power, and no increased absorption is seen when raising laser power to 1.5 mJ.

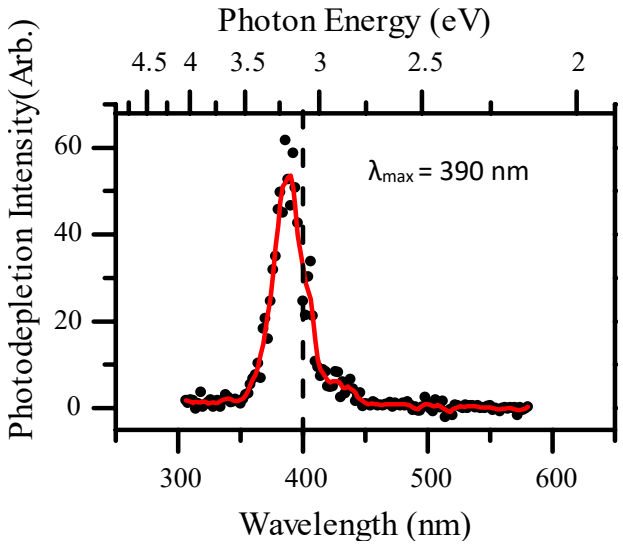

Figure 4.14: *Photodepletion spectra calculated as difference in parent ion intensity between irradiated and non-irradiated $[VOTPP]^+$, calibrated for laser power. 2 nm scan resolution. The solid line represents a three-point adjacent average of the data. The dashed line represents the wavelength switch over on the OPO.*

Ground state and excited state fragmentation again both show a major fragment corresponding to the loss of a phenyl radical at m/z = 603. The MS of this fragmentation is shown in Figure 4.15, and the photofragment spectra of this species is shown below in Figure 4.16.

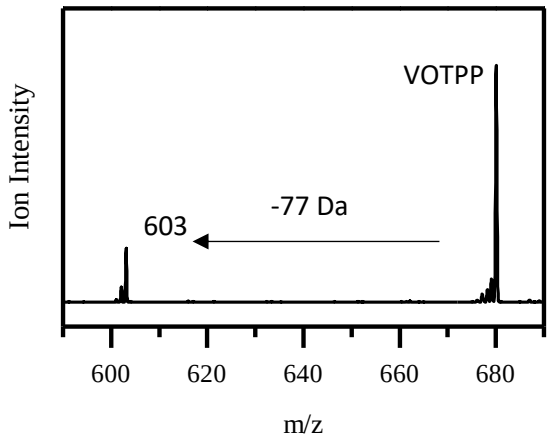

Figure 4.15: *VOTTP ground state fragmentation at 20 % CID voltage, showing the major fragment at m/z = 603.*

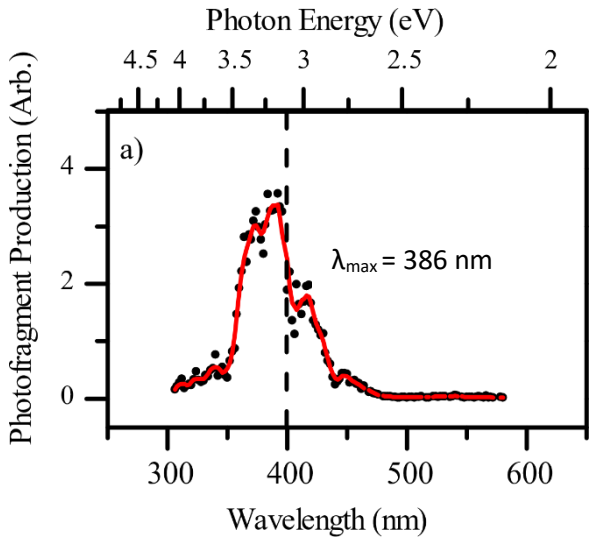

Figure 4.16: *Photofragmentation spectra calculated as difference in parent ion intensity between irradiated and non-irradiated $[VOTPP]^+$, calibrated for laser power for fragment m/z =603. The solid line represents a three-point adjacent average of the data. The dashed line represents the wavelength switch over on the OPO.*

Unlike the other porphyrins studied, the Q band was not enhanced in the photofragment spectra, even when pumped with a higher laser power.

4.5 NiTPP

Nickel is another common metal found in petroporphyrins. A solution phase spectrum of NiTPP was recorded in DCM:MeOH and is shown in figure 4.17. The Soret band was observed at 410 nm, and a single Q band with at 524 nm. The Soret band was notably broader than the other TPP species studied, and like TPP and hemin a broad shoulder was observed on the higher energy side of the peak. This is again assigned as a partially resolved vibronic structure.

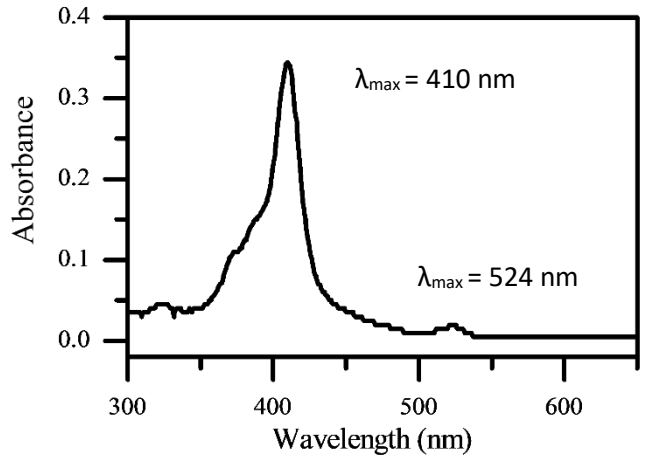

Figure 4.17: *Solution phase UV spectra of NiTPP recorded in DCM:MeOH (80%:20%) at* $1x10^{-5}$ *M concentration.*

As with VOTPP, NiTPP is oxidized in the electrospray and molecular ion peak $[NiTPP]^+$ (m/z =671) is formed. As with all the other metal containing porphyrins, multiple isotope peaks are also resolved in the mass spectrum and only the $[NiTPP]^+$ species is mass selected and analysed. The photodepletion and fragmentation spectra of the major fragment are shown below in Figure 4.18.

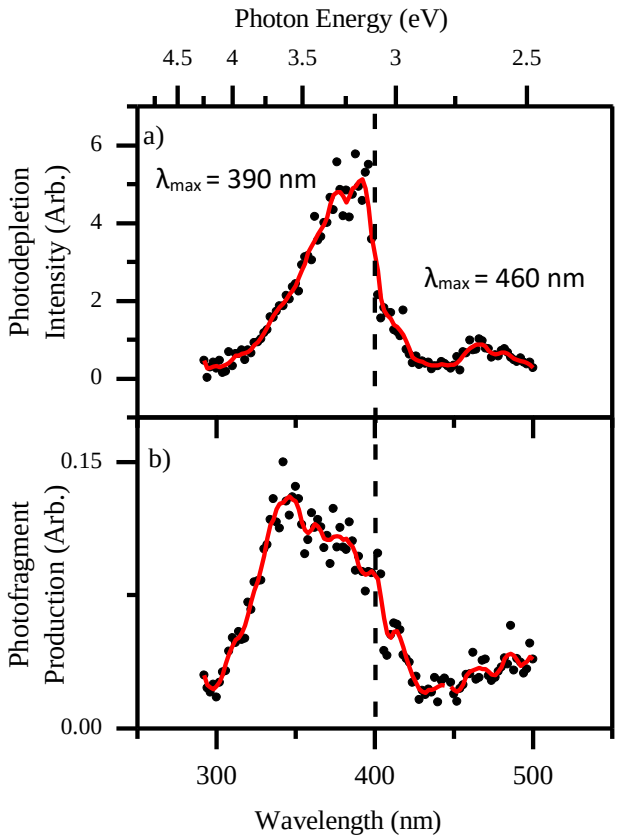

Figure 4.18: *a) Photodepletion spectra calculated as difference in parent ion intensity between irradiated and non-irradiated $[VOTPP]^+$, calibrated for laser power and wavelength, and b) Photofragmentation spectra for fragment m/z =594. The solid line represents a three-point adjacent average of the data. The dashed line represents the wavelength switch over on the OPO.*

As with VOTPP, the gas phase absorption mimics the solution phase with a wide Soret band observed in the solution and gas phase photodepletion spectra. This large trailing band on the blue side of the spectrum is again indicative of multiple vibronic transitions and a vibrationally excited molecule.

4.6 TPP Discussion

The photodepletion and fragmentation spectra of $[TPP+H]^+$, $[FeTPP]^+$, $[VOTPP]^+$ and $[NiTPP]^+$ have all been recorded in the gas phase. The Soret band was well resolved for each species but the Q bands were not clearly resolved at 1 mJ laser power for

the Fe or VO porphyrins. There are three main reasons why this may not be the case. Firstly, the lifetime of the excited species may be longer than the experimental window, and no depletion would occur. Secondly the process may require more power to be seen. Thirdly, the species may be fluorescing, and again producing no depletion. The timescale of the experiment is on the order of milliseconds to seconds, so lifetimes would have to be quite long for this to be a factor. TPP is known to fluoresce but at 650-750 nm, at the far end of the region scanned, so would not affect the spectrum too much. On increasing photon power to 1.5 mJ a Q band feature appeared for the $[FeTPP]^+$ species but not the VO species. It is possible that even at 1.5 mJ, there is not enough energy to pump the Q band, or one of the other processes is preventing the band from being seen.

The observed position of the Soret bands of the MPs all show a blue shift compared to the recorded solution phase spectra. This is in line with Nielsen et al.'s results for heme and chlorophyll, where both Soret bands blue shift in the gas phase compared to results obtained in solution or protein environments. In proteins, the shift is attributed mainly to chlorophyll coupling effects, but solvent shifts can contribute as much as 20 nm shifts in the band position. [51,52] The relative Soret band position in the gas phase and solution are summarised below in Table 4.1:

Table 4.1: *Summary of Soret band shift between solution and gas phase*

Species	Soret Band Solution (nm)	Soret Band Gas Phase (nm)	Soret Band Shift (nm)
TPP	439*	420	-19
FeTPP	396	370	-26
VOTPP	423	390	-33
NiTPP	412	390	-22

*Indicates protic solution

The VOTPP showed the largest Soret band shift, whilst the unmetallated TPP showed the smallest shift. The Q band features also show a similar trend, as summarised in Table 4.2:

Table 4.2: *Summary of Q band shift between solution and gas phase*

Species	Q Band Solution (nm)	Q Band Gas Phase (nm)	Q Band Shift (nm)
TPP	610, 655	550,575	-60, -80
FeTPP	525	522	-3
VOTPP	547	-	-
NiTPP	524	468	-56

For all the species where a Q band was resolved a blue shift was observed between solution and gas phase. As the Q band features are much weaker than the Soret band, they were harder to distinguish. This is summarised in Table 4.3.

Table 4.3: *Summary of Soret band and Q band shift between metal centres in solution and gas phase*

Species	Soret Band GP (nm)	Soret Band Shift from TPP GP(nm)	Soret Band Solution (nm)	Soret Band Shift from TPP Solution (nm)
TPP	420	-	417	-
FeTPP	370	-50	396	-21
VOTPP	390	-30	423	+6
NiTPP	390	-30	412	-5

For all TPP species, the major fragmentation pathway was the loss of a single phenyl radical, forming a characteristic -77 Da peak. This was observed in the ground state with CID and excited state for all TPP porphyrins studied. Unmetallated TPP however showed a large number of low intensity fragments, which were attributed to a long lived triplet state decay pathway. This was much reduced in the Fe, VO and Ni TPP's, suggesting the metal ion reduces this pathway and increases the photo stability of the porphyrin. Whilst this triplet state had been predicted from lifetime analysis of TPP, this experiment has shown empirically the identities of the fragments caused by this triplet state decay and how they vary with respect to wavelength.

4.7 Summary

In all TPP species studied, a blue-shift is observed on moving from the solution phase to gas phase. Gas-phase spectra of the MPs are broadly similar to their respective spectra in solution. The Soret band is well resolved in all porphyrins studied and often required a decreased laser power of 0.5 mJ to be resolved without saturation. The Q-bands conversely were more difficult to resolve, and in most cases, need >1mJ energy

to pump the transition. TPPs fragmentation is dominated by loss of a phenyl radical, in both the ground-state and or excited-state. However, the addition of a metal ion appears to increase photostability of a porphyrin, by preventing a long lived triplet state decay pathway that is seen in unmetallated forms of the respective porphyrins.

4.8 Conclusion

The TPP species studied all electrosprayed with little difficulty and gas phase absorption spectra were recorded, showing the expected shift when moving into the gas phase. Broader than expected Soret bands were observed and these were predicted to be due to vibronic transitions. Spectra recorded in gas phase allow for clearer view of the fundamental absorption properties, away from the effects of bulk solvent. Importantly, this can now be extended to measure the effect of complexing external molecules onto these porphyrins.

Chapter 5: MP complexes

5.1 Introduction:

Chapters 3 and 4 have demonstrated that the spectra of the isolated porphyrin species can be measured in the gas-phase. In this Chapter, we are now able to move on to attempting to measure the spectra of aromatic molecules (e.g. pyridines) complexed to porphyrins. Such complexes are relevant in petrochemistry,[34,35] since they are believed to be present in crude oil samples. It has been suggested by Stoyanov et al. that complexation of an MP with a nitrogen containing aromatic system may reduce the extinction coefficients for absorption in both the Soret and Q-bands of MPs. The aim of the work in this chapter is to directly test this suggestion by forming gas-phase clusters of MPs with nitrogen containing aromatics, and measuring their UV/VIS absorption spectra. These spectra will be directly compared to the spectra of isolated MPs presented in Chapter 4. For our initial studies, we focus here on FeTPPCl, which although it is not a geoporphyrin, was found to electrospray readily in our experimental apparatus to form the charged species $[FeTPP]^+$. This makes it an ideal starting porphyrin to test the gas-phase formation of nitrogen-containing aromatic complexes with porphyrins using electrospray ionisation as a preparative tool. FeTPP is also known to bind to strongly to pyridine in solution, readily forming the 5 then 6 coordinate low spin species [17] with free energies of binding found to be between -4 and – 37 Kj mol^{-1}. [92]

There has been very little previous gas-phase spectroscopic work on clusters between MPs and other molecules. Even and Jortner studied complexes of zinc octaethylporphyrins with a series of small molecules (water, methanol, acetonitrile, benzene and pyridine) that were formed in a pulsed supersonic jet. [45] The electronic transitions of these complexes were studied via laser induced fluorescence across the Q-band region. Even and Jortner observed

red-shifts (reflecting stabilization of the S_1 state) in the origin transitions for the complexes of the clusters with water, acetonitrile and pyridine. They attributed spectral broadening around the origin transitions to the presence of multiple conformations of the clusters in the molecular beam, possible due to different orientations of the ethyl side chains of the porphyrin. Nielsen and co-workers have conducted a limited series of experiments to explore complexation to the heme porphyrin, *i.e.* studying heme$^+$·histidine and heme$^+$·NO. For both clusters, they found that complexation did not perturb the electronic transitions to the Soret or Q-bands. [93,94]

5.2 Experimental Method:

As discussed above, the optimum solvent system used to form FeTPPCl via electrospray was 80% DCM:20% MeOH. This gave a good solubility for the porphyrin and the MeOH allowed for an efficient ESI process. When initially looking for clusters however, by adding drops of the clustering molecule (i.e. pyridine), no porphyrin-pyridine clusters were observed. This may be due to the MeOH and DCM clustering around the porphyrin and preventing it from interacting with other molecules. In contrast, we found that using acetonitrile (MeCN) as a solvent allowed clusters of the porphyrin with pyridine to be formed in substantial quantities. FeTPPCl is moderately soluble in MeCN, and required minor sonication to produce a solution that was suitable for electrospraying.

In a 4 ml sample vial, 3 ml of 1 x 10^{-6} M FeTPPCl in MeCN was mixed with 30 µl of 1 x 10^{-3} pyridine in MeCN and sonicated to ensure mixing. To maximise cluster formation trapping conditions were altered to increase the “softness” of the ionisation. This included decreasing the temperature of the capillary and reducing the volume and pressure of drying gas used.

5.3 FeTPP. Pyridine: Results and Discussion

Cluster formation of $FeTPP^{+}$·pyridine (m/z = 747) was apparent in the total ion mass spectrum observed following electrospray of a solution prepared as described above. The cluster peak was several times more intense than the bare $FeTPP^{+}$ peak.

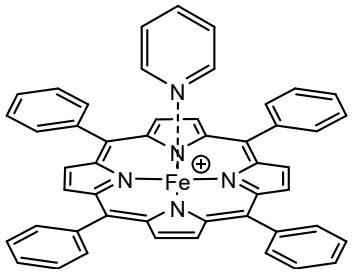

Figure 5.1: *Possible structure of [FeTPP·Pyridine]$^{+}$ complex, illustrating direct interaction of the pyridine nitrogen with the metal centre of the porphyrin.*

However, the $FeTPP^{+}$.Pyridine mass spectral peak was observed to sharply decrease in intensity when an isolation width below 2.0 m/z units was employed. This is due to the ion trapping process, which can break apart a metastable cluster ion. To perform further experiments, an isolation width of 2.0 m/z = units was therefore used, but a consequence of this wider isolation width was that different isotopic species were present in the ion packet selected (see Figure 4.8 for the isotopic distribution of m/z = peaks for $FeTPP^{+}$), and subsequently subjected to laser interrogation. This can be clearly seen in the CID mass spectrum shown in Figure 5.2, where the parent ion peak is substantially broadened.

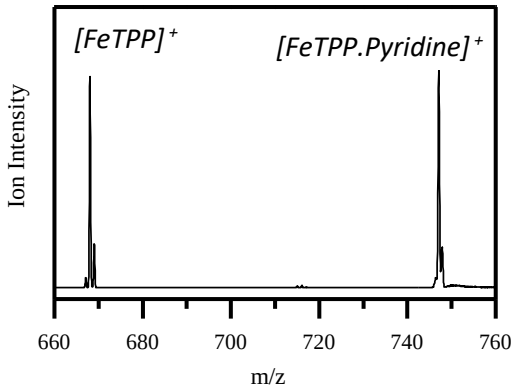

Figure 5.2 *CID MS of [FeTPP.Pyridine]+ recorded at 0.1 V (4%) CID intensity, showing the cluster fragmenting via cluster fission with production of the FeTPP+ cation.*

Further evidence that the FeTPP$^+$·pyridine cluster formed via electrospray is only metastable is that the collisional energy required to fragment the cluster was far lower than that required to induce fragmentation in other ionic complexes studied in similar work. [95,96]

As cluster dissociation appears to occur at much lower energies than for other species, in particular the isolated porphyrins studied in Chapters 3 and 4, the power of the laser used for the photodissociation experiments had to be reduced to avoid saturation. (Saturation occurs in our experiment when the laser on signal records a zero or > 99 % decrease in ion intensity compared to the laser off signal, and results in a flat line being observed in the resulting photodepletion spectra.) A power study was performed on the cluster and saturation was observed for laser powers above 0.4 mJ. (This was done by observing the region where photodepletion was approaching 100%.) A laser power of 0.3 mJ was therefore used for the spectra presented below as this gave a depletion of ~90% at the λ_{max} and no saturation. The power could not accurately be measured any lower than this as it was decreased by detuning the laser and this affects the shape and profile of the laser beam. In future work, it will be necessary to reproduce the experiments performed here using neutral density filters to reduce the laser power in a more controlled manner.

The photodepletion and photofragmentation spectra of $FeTPP^+$.pyridine were measured between 290 and 550 nm, with the results being shown below in Figures 5.3 and 5.4.

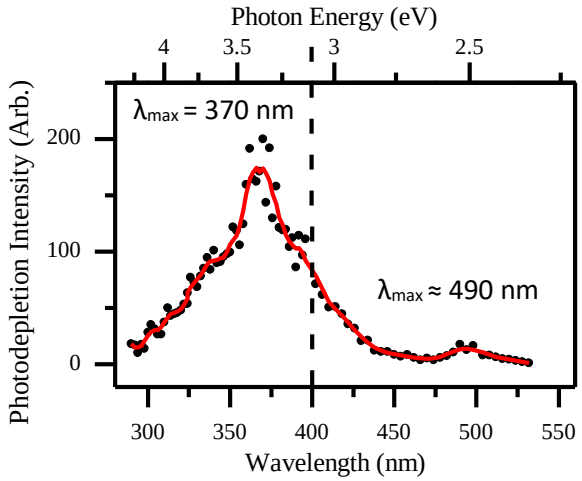

Figure 5.3: *Photodepletion spectra calculated as difference in parent ion intensity between irradiated and non-irradiated [$FeTPP^+$.Pyridine], calibrated for laser power. 2 nm scan below 400nm and 4nm scan above 400nm. The solid line represents a three point adjacent average of the data. The dashed line represents the wavelength switch over on the OPO.*

The photodepletion spectrum (Figure 5.3) shows a broadened Soret band with λ_{max} = 370 nm, and a weaker Q band feature at λ_{max} = 490. (The FWHM of the Soret band is approximately 60 nm, compared to approximately 30 nm for the uncomplexed $FeTPP^+$ cation, Figure 4.9. Shoulders to the main Soret band also appear at both the high and low side of the band, at approximately 335 and 390 nm. Although efforts were made in setting up this experiment to avoid saturation, our experience with other systems informs us that the numerical photodepletion intensity is at a level where we expect photodepletion may still be saturated. Due to time constraints at this stage of the project, it was not possible to revisit this issue experimentally. In future work, it will certainly be necessary to repeat these experiments with lower laser power. However, this issue constitutes an important result for this work, since it reveals that there is no dramatic fall off in the extinction coefficient upon complexation of the metalloporphyrin with the nitrogen containing aromatic.

The λ_{max} = 370 nm for the Soret band feature of $FeTPP^+$.pyridine assessed from the spectrum presented in Figure 5.3 can be compared to the λ_{max} = 382 nm for the Soret band feature of the uncomplexed $FeTPP^+$. Comparing the Q-bands, the cluster Q-band has been assigned a λ_{max} = 490 nm, while the bare $FeTPP^+$ was assigned a λ_{max} = 516 nm. These values indicate that the cluster transition is blue-shifted compared to the monomer, an unexpected result given that Even and Jortner recorded Q-band red-shifts for their zinc-porphyrin-molecule complexes. Indeed, a red-shift would typically be expected for electronic excitations upon complexation of an ionic molecule to a polar solvent. Possible explanations for the discrepancy observed here may be i) the inherent difficulty in measuring the spectra around the Soret band region due to it appearing in the vicinity of the crystal change over point in the OPO, and ii) low signal-to-noise in the Q-band region obscuring the true position of the origin transition. It would be useful in future work to perform TDDFT calculations of both uncomplexed $FeTPP^+$, and the $FeTPP^+$.pyridine cluster, to obtain a theoretical prediction for the spectral shifts expected for the Soret and Q-bands.

It is interesting to consider the overall profile of the photodepletion band (Figure 5.3) in the context of the origin bands measured by the high-resolution study of Zn porphyrins by Even and Jortner. They observed evidence for the origin transition being split into three bands, with the central band being the most intense. They assigned this splitting as being due to the presence of multiple cluster isomers, or to low frequency vibrations of the alkyl side chains of the porphyrin. The spectrum displayed in Figure 5.3 may well display a similar profile, as it appears to be composed of a stronger central feature (λ_{max}= 370 nm) and two side bands with (tentative) λ_{max}= 335 and 390 nm.

Next we turn to discussing the photofragmentation behaviour of the cluster. Unsurprisingly, the major photofragment following photoexcitation of $FeTPP^+$.Pyridine is the $[FeTPP]^+$ cation, formed via simple cluster fission:

$$FeTPP.pyridine^+ + h\nu \rightarrow [FeTPP]^+ + pyridine \quad \text{[Equation 5.1]}$$

A second, minor photofragmentation channel is also observed corresponding to loss of a m/z = 77 neutral from $[FeTPP]^+$; this fragment has been observed upon photoexcitation of the bare $FeTPP^+$ (Chapter 5), and may well be formed by multiphoton excitation of the cluster, either by simultaneous absorption of two photons [5.2a] or from sequential absorption of two photons [5.2b]:

$$FeTPP.pyridine^+ + 2h\nu \rightarrow [FeTPP - m/z=77]^+ + m/z = 77 + pyridine \quad \text{[Equation 5.2a]}$$

$$FeTPP.pyridine^+ + h\nu \rightarrow [FeTPP]^+ + pyridine$$

$$\rightarrow [FeTPP - m/z =77]^+ + m/z = 77 + pyridine \quad \text{[Equation 5.2b]}$$

Indeed, the differences in the spectral profiles of the $[FeTPP]^+$ photofragment and the $[FeTPP - mz=77]^+$ photofragment further suggests that the two photofragments are formed via different multiphoton processes.

The Soret band in the photodepletion spectrum (Figure 5.3) shows a distinct shoulder feature centred at 335 nm. This feature can also be seen in the $[FeTPP]^+$ photofragment action spectrum, but not in the action spectrum of the $[FeTPP - m/z = 77]^+$ fragment. This is consistent with the $[FeTPP]^+$ photofragment being a primary photofragment obtained from direct excitation of the cluster. In contrast, the $[FeTPP - m/z = 77]^+$ action spectrum appears to display a broad shoulder to lower energies which is centred around 400 nm.

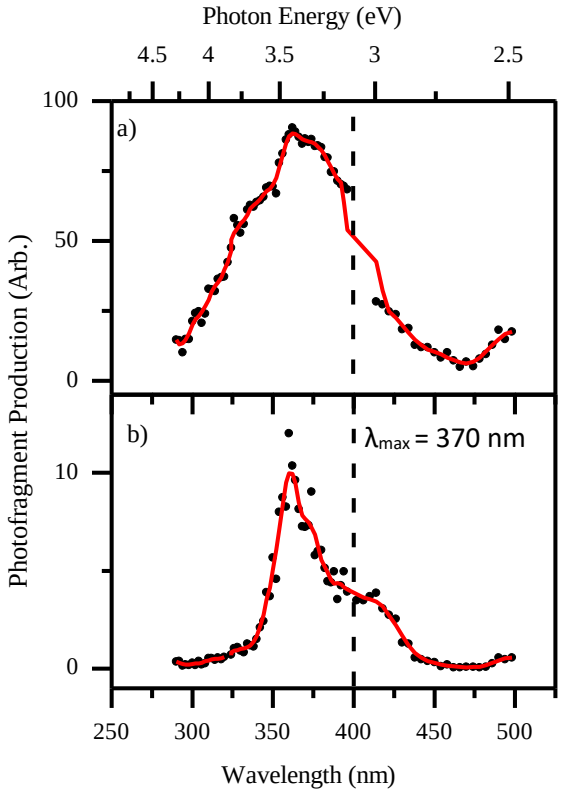

Figure 5.4: *Photofragmentation spectra of [FeTPP.Pyridine]⁺, calibrated for laser power for the a) m/z =668 ([FeTPP]⁺) and b) m/z = 591 photofragments. The solid line represents a three-point adjacent average, with the dashed line representing the OPO wavelength switch.*

5.4 FeTPP.quinoline: Results and Discussion

The $FeTPP^+$.quinoline cluster was produced using a similar electrospray protocol to that used for the $FeTPP^+$·pyridine cluster. The proposed structure of the complex is shown in Figure 5.5. $FeTPP^+$·quinoline again required a wider isolation window to ensure the complex was not broken apart. As with the $FeTPP^+$·pyridine cluster, the collisional energy necessary to induce cluster fragmentation (4% CID) was much lower than the uncomplexed $[FeTPP]^+$ ion, or for other stable molecular clusters that have been studied previously in our group. To compensate for the weak binding of the $FeTPP^+$·quinoline cluster, the laser intensity was reduced to 0.3 mJ to attempt to prevent saturation.

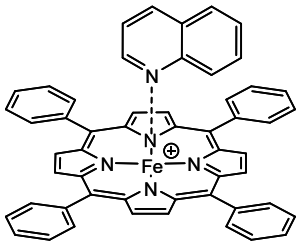

Figure 5.5: *A suggested structure for the FeTPP⁺·quinoline complex.*

The photodepletion spectrum for FeTPP⁺·quinoline is displayed in Figure 5.6. An intense Soret band was again observed centred for this cluster with λ_{max} = 370 nm, a value that is effectively the same as that measured for the FeTPP⁺·pyridine cluster. The peak broadening that was observed for the FeTPP⁺·pyridine cluster (compared to the spectrum of uncomplexed FeTPP⁺) was again observed for FeTPP⁺·quinoline. A weaker absorption feature can be observed at higher-energies, which can be assigned to the Q-band. This band appears to have a λ_{max} = 510 nm for FeTPP⁺·quinoline.

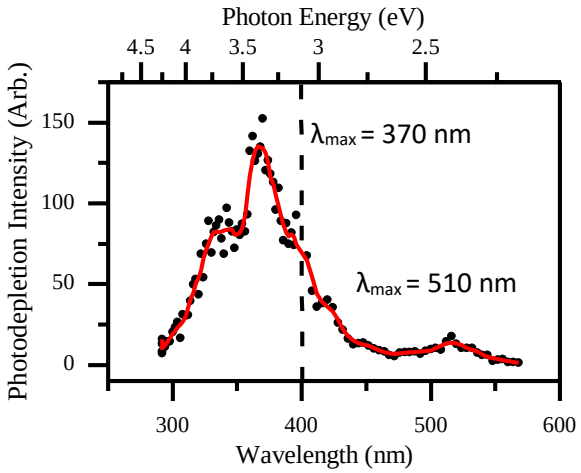

Figure 5.6: *Photodepletion spectra calculated as the difference in parent ion intensity between irradiated and non-irradiated FeTPP⁺·quinoline, calibrated for laser power. A 2 nm laser scan step size was used below 400nm and a 4nm laser scan step size for energies above 400nm. The solid line represents a three-point adjacent average of the data. The dashed line represents the OPO wavelength switch over point.*

The photofragmentation behaviour of the $FeTPP^+$·quinoline cluster closely follows that of the $FeTPP^+$·pyridine cluster, with the major photofragment pathway being cluster fission as evidenced by formation of the $[FeTPP]^+$ ion (m/z = 538):

$$FeTPP^+ \cdot quinoline + h\nu \rightarrow FeTPP^+ + quinoline \qquad \text{[Equation 5.3]}$$

As for the $FeTPP^+$·pyridine cluster, a minor fragment corresponding to $[FeTPP]^+$ - 77 m/z = units (m/z = 461) is also observed upon photoexcitation of $FeTPP^+$·quinoline in the region of the Soret band, and can be attributed to secondary processes.

Figure 5.7 displays the photofragment action spectra for the m/z =538 and m/z =461 photofragments of $FeTPP^+$·quinoline. The Soret band is however clearly saturated in this photofragment spectrum as the $[FeTPP]^+$ ion production was around 100%. There may therefore be further spectral structure present for this band, which has been lost in the current study. As the minor fragment, $[FeTPP]^+$ - 77 Da, is produced with lower intensity, the overall band profile should be more reliable for this photofragment.

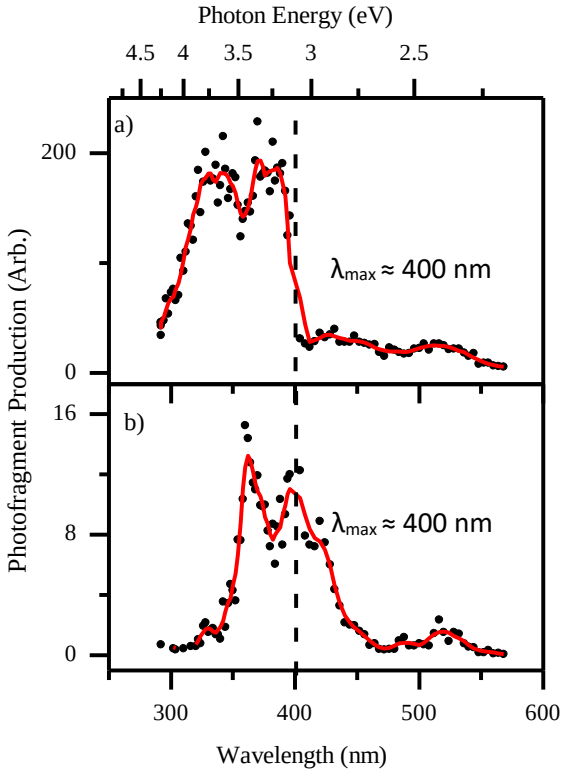

Figure 5.7: *a) Photofragmentation spectra of FeTPP$^+$·quinoline for a) the major photofragment (m/z =538) and b) the minor photofragment (m/z = 461). The solid line represents a three-point adjacent average, with the dashed line representing the OPO wavelength switch over point.*

5.5 VOTPP.Quinoline: Results and Discussion

As Fe-centred geoporphyrins are not common, it was desirable to study a vanadium or nickel geoporphyrin. The relatively inert structure of the D_{4h} NiTPP and octaethyl etioporphyrin (OEP) molecules made cluster formation difficult in the ESI source, so VOTPP was chosen for study. Previous experimental work by Stoyanov et al. has been performed on the formation constants of vanadyl OEP and pyridine using photochemical titration.[40] They found that the formation constants for vanadyl pyridine and isoquinoline complexes were higher than that of nickel complexes, showing vanadyl porphyrin clusters are more inert. This would suggest why these clusters were more readily formed in the electrospray source.

As VOTPP was poorly soluble in MeCN, a mixed solvent (50:50 MeCN:toluene) was used to produce the precursor solution for this series of experiments. This solution was sonicated for 10 minutes to aid dissolution of the porphyrin.

Figure 5.8 displays the gas-phase absorption spectrum of the $VOTPP^+$·quinoline cluster. The photodepletion spectrum shows an intense Soret band centred at 402 nm, with no visible Q band features. The $VOTPP^+$ photodepletion spectrum (Figure 4.23) was notably sharper when compared to other MPs (Chapter 4), and this is seen again in the $VOTPP^+$·quinoline cluster. As with the $[FeTPP]^+$ clusters studied above, the Soret band of $VOTPP^+$·quinoline is widened compared to uncomplexed $VOTPP^+$.

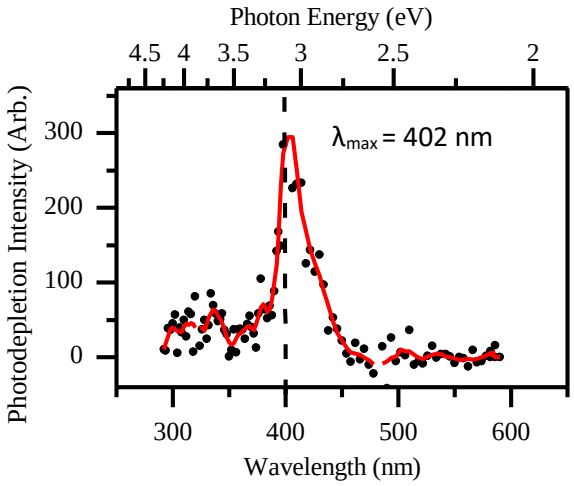

Figure 5.8: *Photodepletion spectrum of $VOTPP^+$·quinoline. A 2 nm laser step size was employed below 400nm and a 4nm laser step size above 400 nm. The solid line represents a three-point adjacent data average, and the dashed line represents the OPO wavelength switch over point.*

Stoyanov et al. have recorded solution phase spectra of VOTTP and pyridine, quinoline and isoquinoline, along with computationally predicted excited states. [40] They found negligible shifts when adding quinoline to VOTPP, with the Soret band maxima remaining at 406 nm. When isolated in the gas phase, the Soret band for $[VOTPP]^+$ is 390 nm, and when complexed

to quinoline is 402 nm, a small redshift. This shift is in the opposite direction to the calculations performed by Stoyanov where the Soret band was predicted at 389 nm.

The only strong photofragmentation pathway observed upon photoexcitation of $VOTPP^{+}$·quinoline corresponds to cluster fission with formation of the $[VOTPP]^{+}$ cation:

$$VOTPP^{+}\cdot quinoline + h\nu \rightarrow VOTPP^{+} + quinoline \qquad \text{[Equation 5.4]}$$

Figure 5.9 displays the photofragment action spectrum for $[VOTPP]^{+}$ from $VOTPP^{+}$·quinoline. Intriguingly, the photofragment action spectrum does display a weak feature at 490 nm, consistent with the Q-band. This feature may not have been observed in the photodepletion spectrum (Figure 5.8) due to low signal noise around 500 nm in this spectrum.

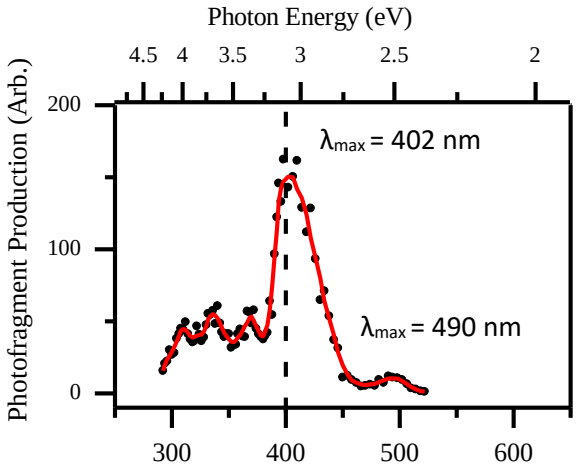

Figure 5.9: *Photofragmentation spectrum of the $[VOTPP]^{+}$ photofragment (m/z = 680) from $VOTPP^{+}$·quinoline. The solid line represents a three-point adjacent average of the data. The dashed line represents the wavelength switch over on the OPO.*

The Soret band in the photofragment spectra is notably asymmetrical with 3 weakly resolved peaks between 300 and 375 nm. Solution phase spectra obtained by Stoyanov et al. show a significant tailing effect towards the higher energies with VOTPP and isoquinoline and this may be a similar effect. [35]

5.6 Further Discussion:

All of the MP^+·nitrogen aromatic clusters studied in this Chapter could be formed with relative ease using electrospray ionization. Strong ion signals were attributed to the complex, and CID studies readily confirmed the identity of these peaks. By far the most striking feature observed in the photodissociation spectra of the MP-clusters was the strong intensity of the Soret band that is maintained through complexation. This meant that the initial spectra presented here suffer from saturation effects. However, it is possible to conclude that there is no significant weakening of the transition intensity upon complexation of MPs with nitrogen heteroaromatics. In addition, the broadening of the Soret band in the cluster spectra is notable. This broadening appears to scale in line with the band shapes for the uncomplexed MP spectra, since the $[VOTPP.quinoline]^+$ Soret band displays the narrowest Soret peak, as does the $VOTPP^+$ cation.

The results from the $FeTPP^+$ clusters will be further discussed first, with the Soret band shifts and peak broadenings (FWHM) being summarised in Table 5.1:

Table 5.1: *Summary of Soret band shifts for clusters of $FeTPP^+$ with pyridine and quinoline.*

Species	**Soret Band (nm)**	**Shift from Soret band of MP^+**	**Soret band width (FWHM)**
$[FeTPP]^+$	420	-	40
$[FeTPP.Pyridine]^+$	370	-50	80
$[FeTPP.Qunoline]^+$	370	-50	75

It is clear that complexation of $FeTPP^+$ with both pyridine and quinoline induces a large blueshift in the Soret band. In addition, complexation induces a large broadening of the

Soret band, with both cluster species showing a significantly broader peak. The spectral broadening may reflect relatively high internal energies for the clusters, which would be consistent with metastable species.

A comparison of the Q bands of the clusters with the Q band of the monomer, also reveals a blue spectral shift, which is more pronounced in the $[FeTPP.Pyridine]^+$ cluster. It is not possible to tabulate changes in the increase in Q-band width due to the relatively weak spectral signal over this region. Table 5.2 summarises the Q band shifts on complexation.

Table 5.2: *Summary of Q band shifts for clusters of $FeTPP^+$ with pyridine and quinoline.*

Species	**Q Band (nm)**	**Q-Band Shift from un-clustered**
$[FeTPP]^+$	~560	-
$[FeTPP.\ Pyridine]^+$	495	-65
$[FeTPP.\ Qunoline]^+$	510	-50

Finally, Table 5.3 summarises the results for the $VOTPP^+$·quinoline cluster. The tabulated results for the vanadium porphyrin cluster show little change in the Soret band width, and a red spectral shift for the Soret band of the cluster compared to the monomer.

Table 5.3: *Summary of $VOTPP^+$ and $VOTPP^+$·quinoline results*

Species	**Soret Band (nm)**	**Q Band/s (nm)**	**Soret Band Shift from un-clustered**	**Q band shift from un-clustered**	**Soret Band Width (FWHM)**
$VOTPP^+$	390	-	-	-	36
$VOTPP^+$·quinoline	402	490	+12	-	40

This blue-shift in the Q-band positions for the Fe porphyrin complexes is highly surprising considering the results of Even and Jortner who observed strong red-shifts when pyridine complexed to an (albeit uncharged) zinc MP. [50] Indeed, the rather small red-shift observed for $VOTPP^+$·quinoline is also surprising. However, Nielsen and co-workers observed little spectral shift in the heme bands upon complexation with histidine and NO. [92,93] This is of note as the porphyrin clusters studied by Nielsen et al. are also prepared by via electrospray ionization. As the clusters in the study of Even and Jortner were produced in a supersonic expansion, they can be expected to be cold, so the spectra should be more reliable than those of the hot, metastable clusters investigated here.

The observed blue shift when moving from solution to the cluster in gas phase may also be affected by a change in Franck-Condon factor when moving from the monomer to the cluster. This could be shown to be the case if vibrationally resolved spectra were recorded, but this would require much cooler ions than are currently present in the ion trap.

5.7 Conclusions

This work presented in this chapter illustrates that electrospray ionization can be used to produce gas-phase clusters of MPs and nitrogen heteroaromatics. In this preliminary work,

it has been possible to identify the regions where the Soret and Q-bands appear for these clusters, but it will be necessary to refine these measurements while effectively controlling for saturation effects. The major result to emerge from this study is that the Soret band absorptions of MPs complexed to nitrogen heteroaromatics remain very strong, hence leading to the saturation effects observed here. This seems to disprove the theory put forward by Stoyanov et al. that the reduction in the absorption intensity of MPs in crude oil samples arises due to complexation with nitrogen containing aromatics

Chapter 6: Conclusions and Future Work

6.1 Conclusions

The work reported in this thesis has shown the viability of using gas-phase action spectroscopy techniques for studying the electronic spectroscopy and photochemistry of porphyrin molecules, as well as their complexes with nitrogen containing aromatic molecules. The photodepletion spectra can be interpreted as being equivalent to total absorption spectra assuming that no florescence is occurring. To this extent the expected main spectral features that appear in solution-phase UV/Vis spectroscopy of porphyrins (i.e. Soret and Q-bands) are readily identifiable in the gas-phase spectra acquired in this work. The results are in line with other similar experiments such as those performed by Nielsen et al. [52,55,56]

Photofragmentation of the non-metallated porphyrin, TPP, led to two major (intense) photofragments corresponding to loss of one or two phenyl radicals from the protonated TPP species, as well as a considerable number of additional, low intensity photofragments. The production of these low intensity photofragments was assigned to a decay pathway that followed from a triplet state, with a lifetime that is considerably longer than the lifetime of the singlet excited state, which appears to lead to production of the two most intense photofragments. Evidence for excited state decay from the triplet excited state was found to be most intense close to the Soret band maxima. Overall, the measurements conducted in this thesis

provided direct evidence that $TPP{\cdot}H^+$ is photo-unstable, since it degrades into a considerable number of (non-ergodic) photoproducts following photoexcitation.

This situation contrasted dramatically with the spectroscopy and photochemistry that was observed when the metal centred porphyrins were studied across the same spectral region. The fragmentation pathways observed for the metalloporphyrins were largely ergodic, and very few different photofragments were observed. Indeed, a primary analysis suggests that the minor photofragments observed from the metalloporphyrin systems result from multiphoton effects. These results are consistent with the known increase in molecular stability that results from the incorporation of a metal centre in a porphyrin molecule. Whilst the Soret band remained strongly present in all the MP spectra recorded, the similarities to solution phase spectra were less clear. Q bands were considerably more difficult to resolve and required more power for transitions to be observed. Whilst the Soret band was still clearly observable, it was typical broader and less symmetrical, indicating a high degree of vibrational excitation.

Porphyrin clusters with small nitrogen-containing aromatic molecules were formed with relative ease in the experimental apparatus using electrospray ionization, and gave rise to strong photodissociation cross sections. For the metalloporphyrin cluster species studied in this work, the Soret band was still a very strong spectral feature, such that this band was saturated under the experimental conditions used in this preliminary work (even at reduced laser powers compared to those usually employed in our group). This observation is important as it directly contradicts the suggestion of Stoyanov et al., who proposed that axial coordination of a metalloporphyrin by

small nitrogen containing aromatic molecules leads to a dramatic reduction in the spectroscopic intensity of the Soret band. In addition, the results presented here suggest a notable peak broadening and spectral blue shift of the Soret band for the complexes compared to the isolated metalloporphyrins. This spectral band broadening is consistent with a cluster species that has a high internal energy.

The experimental setup does not provide any cooling to the ions, only the collisions with He buffer gas present in the QIT. Because of this, ions will be no cooler than room temperature, making vibrational levels very difficult to distinguish. Broadening of the Soret band was observed for $TPP.H^+$ and $FeTPP^+$ and was assigned as an unresolved vibronic structure. Being able to cool the ions would help provide more information. Combinations of ESI sources and cryogenically cooled ion traps are known, with Rizzo et al. combining a nanospray source with a cryogenic multipole rf ion trap to obtain action spectra. [97] The ions are cooled to roughly 10 K and this enabled vibrational detail to be clearly resolved. This would clearly also have the advantage of resolving the vibrational states on the blue side of the Soret band. It would also be useful to acquire the Zn MP-pyridine gas-phase absorption spectrum recorded by Even et al. in our instrument, as this would allow a direct comparison of results. It would also be very valuable to conduct TD-DFT calculations on these clusters to determine whether red or blue-shifts are expected.

6.2 Future work

One major area that should be explored in future work is the application of quantum chemistry to the molecules and complexes studied here. It would be very useful to use DFT methods, along with TD-DFT calculations to predict the Soret and Q- band

positions for the uncomplexed and complexed metalloporphyrins to obtain a theoretical prediction of the spectral shifts that could be expected across both spectral bands. Some preliminary work along these lines was carried out as part of this research project, but the size of the molecular systems and the presence of the metal centres makes these calculations challenging.

One significant experimental difficulty faced in this research project was that to isolate the clusters of porphyrins with aromatic molecules in the quadrupole ion trap (essential for laser interrogation) a large isolation window was required. This was attributed to the metastable nature of the clusters, which are produced at ambient temperatures in the electrospray source and are not cooled as in supersonic beam experiments. The isolation procedure would cause cluster fragmentation with isolation widths less than 2 m/z units. This situation may have reduced the resolution of the spectra recorded in this work. This could potentially be improved in future work by spending more time tuning the parameters in the mass spectrometer software. Alternatively, a different method of introducing the complexing molecule to the electrospray source could be used, such as adding it to the drying gas in the ESI source region, or directly into the ion trap.

Another experimental concern encountered in this work was the strong intensity of the Soret band in the experiments on the complexed and uncomplexed porphyrin species. To avoid saturation, the laser had to be detuned to an extent that the laser beam shape was adversely affected. One way that this can be avoided in future work is by using neutral density filters, to decrease the power of the laser but maintain its

beam shape and position. This should then allow for spectra of the complexed porphyrin to be acquired with better signal-to-noise ratios.

Finally, the main objective of this work was to observe how the Soret band was affected when complexes with small aromatic molecules were formed. Although a widening of the Soret peak was observed, along with a blueshift, the Soret band remained a very intense spectral feature, unlike in the situation in crude oils where it seems to be greatly diminished. It would therefore be of interest to see how other complexing molecules affect the Soret band intensity. This could be other small aromatic molecules that are present in oil, or larger molecules, more akin to the asphaltene type molecules that are known to be present in significant concentrations in crude oil samples.

Appendix

A 1.1 Introduction

Preliminary results were also recorded for a second type of porphyrin molecule, the octaeythyl porphyrins. These are another class of porphyrin molecules that are found as geoporphyrins. Unlike the TPP's they are substituted at the alpha positions with ethyl groups.

A 1.2 Nickel Octaethyl Porphyrin

Photodepletion and photofragmentation spectra were recoded for NiOEP. The major fragment was accounted for by the fragmentation of one of the octaethyl side chains.

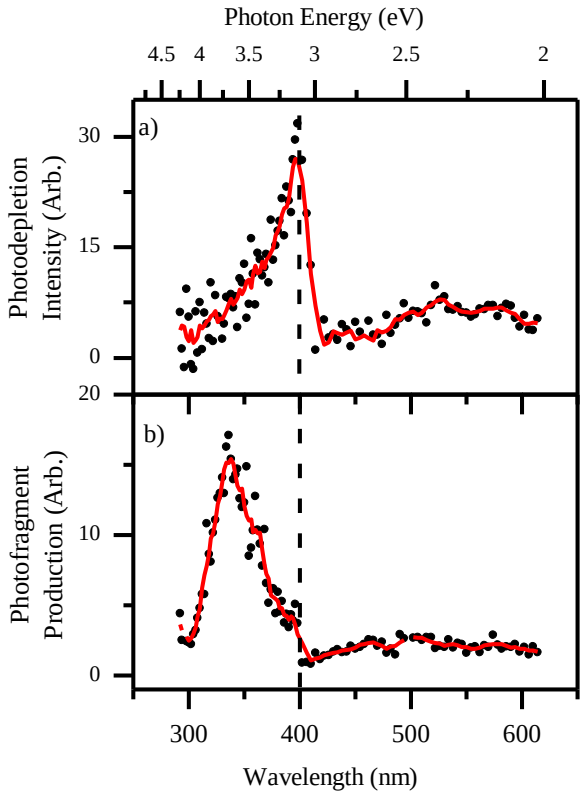

Figure A 1 : *a) Photodepletion spectra and b) Photofragmentation spectra calculated as difference in parent ion intensity between irradiated and non-irradiated $[NiOEP]^+$, calibrated for laser power. 2 nm scan resolution. The solid line represents a three-point adjacent average of the data. The dashed line represents the wavelength switch over on the OPO.*

A 1.3 Vanadium Octaethyl Porphyrin

The photodepletion and photofragmentation spectra of VOOEP are shown below. The Soret band is uncharacteristically broad and poorly resolved. The photofragment spectra revels a clearer absorption cross section, with λ_{max} = 340 nm.

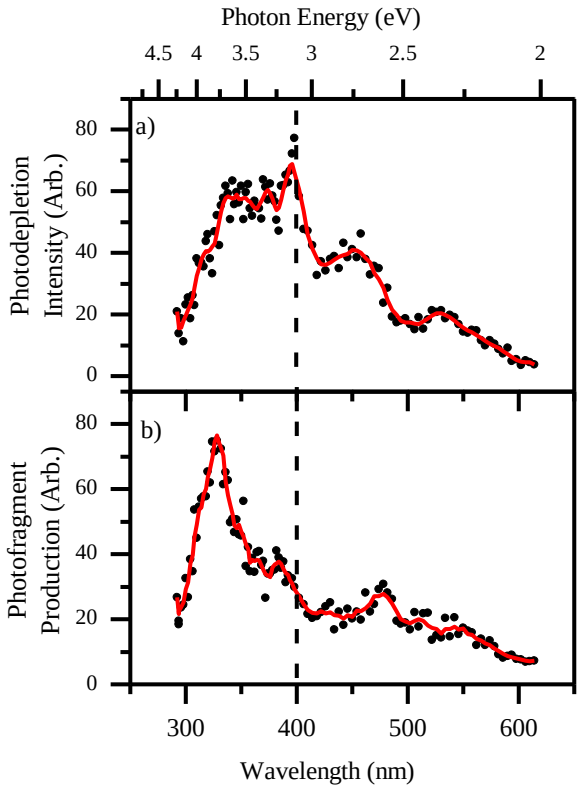

Figure A 2: *a) Photodepletion spectra and b) Photofragmentation spectra calculated as difference in parent ion intensity between irradiated and non-irradiated $[VOOEP]^+$, calibrated for laser power. 2 nm scan resolution. The solid line represents a three-point adjacent average of the data. The dashed line represents the wavelength switch over on the OPO.*

The Soret band and Q band positions are summarised in Table A1, along with Soret band shift from solution phase spectra.

Table A.1 *Soret and Q band positions of Octaethyl porphyrins*

Species	Soret Band (nm)	Q Band/s (nm)	Soret Shift from Solution
VOOEP	~400	490	~ -5
NiOEP	396	520	+ 6

A 1.4 Vanadium Octaethyl Porphyrin.Quinoline Complex

A cluster ion was formed between VOOEP and quinoline which electrosprayed with good intensity. The complex was however quite unstable, and absorption bands were significantly broadened.

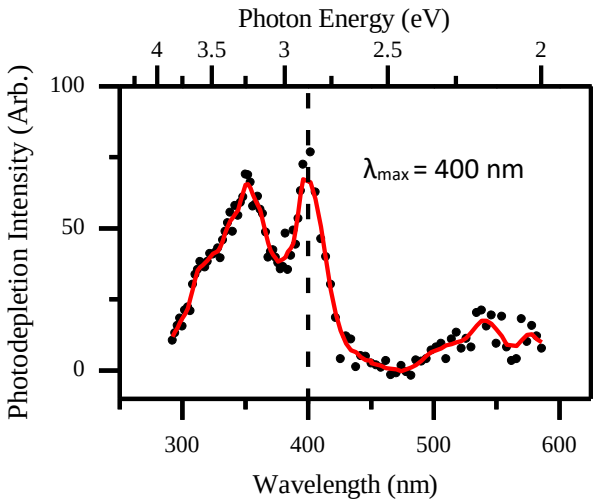

Figure A 3: *Photodepletion spectra calculated as difference in parent ion intensity between irradiated and non-irradiated [VOOEP.Quinoline]$^+$, calibrated for laser power. 2 nm scan below 400nm and 4nm scan above 400nm. The solid line represents a three point adjacent average of the data. The dashed line represents the wavelength switch over on the OPO.*

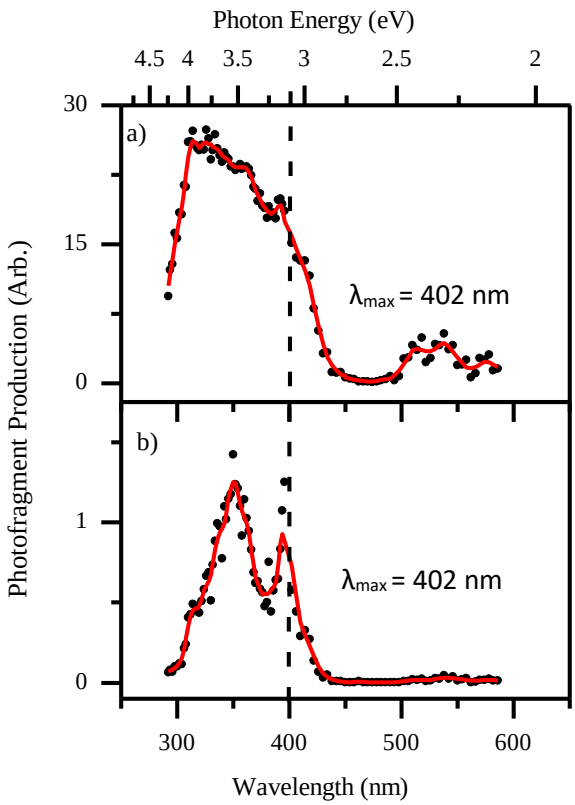

Figure A 4: *a) Photofragmentation spectra calculated as difference in parent ion intensity between irradiated and non-irradiated $[TPP.H]^+$ calibrated for laser power for a) fragment m/z =538 and b) m/z = 461. The solid line represents a three-point adjacent average of the data. The dashed line represents the wavelength switch over on the OPO.*

Concluding Remarks

These initial results show that the experimental technique can be applied to other porphyrin systems, including the formation of clusters. The difficulties faced with recording these spectra also emphasis the importance of controlling the both the ion trapping in the QIT and laser power, both of which are cover in the future work section.

List of abbreviations

CID – Collision Induced Dissociation

CRM – Charge residue model

DFT – Density functional theory

FETPP – Iron tetraphenyl porphyrin

HOMO – Highest occupied molecular orbital

IEM – Induced emission model

LUMO – Lowest unoccupied molecular orbital

MeCN – Acetonitrile

MeOH – Methanol

MP – Metalloporphyrin

MS – Mass Spectrometry

Nd:YAG - Neodymium-doped yttrium aluminium garnet

NIOEP – Nickel octaethyl porphyrin

NiTPP – Nickel tetraphenyl porphyrin

OEP – Octaethyl porphyrin

OPO – Optical paramagnetic oscillator

QIT – Quadrupole ion trap

REMPI – Resonant enhanced multi photon ionisation

TD-DFT – Time dependent density functional theory

TMA – Tetramethylammonium

TOF-MS – Time of flight mass spectrometry

TPP – Tetraphenyl porphyrin

VOOEP - Vanadium octaethyl porphyrin

VOTPP – Vanadyl tetraphenyl porphyrin

Bibliography

1. C. D. Windle, M.W. George, R. N. Perutz, P. A. Summers, X. Z. Sun and A. C. Whitwood, *Chem. Sci*., 2015, **6**, 6847
2. J. Willkomm, K. L. Orchard, A. Reynal, E. Pastor, J. R. Durrant and E. Reisner, *Chem. Soc. Rev.*, 2016, **45**, 9-23
3. M. Urbani, M. Grätzel, M.K. Nazeeruddin, T. Torres, *Chem. Rev.*, 2014, 114, **24**, 12330–12396
4. S. Rühle, M. Greenshtein, S.G. Chen, A. Merson, H. Pizem, C. S. Sukenik, D. Cahen, and A Zaban, *J. Phys. Chem. B*, 2005, **109**, 5397–15409
5. M. T. Huggett, M. Jermyn, A. Gillams, R. Illing , S. Mosse, M. Novelli, E. Kent, S. G. Bown, T. Hasan, B. W. Pogue and S. P. Pereira, *Brit. J. Cancer, 2014,* **110**, 1698–1704
6. F. Hamon , P. Goeminne, *Semin. Ophthalmol.* 2001 ,**16**, 223-232
7. A. Treibs*, Liebigs, Ann. Chem*. 1934, **509**, 103−114.
8. A. Treibs, *Liebigs, Ann. Chem*. 1934, **510**, 42−62.
9. A. Treibs, D. Dinelli, *Liebigs Ann. Chem*. 1935, **517**, 170−172.
10. A. Treibs, *Liebigs, Ann. Chem.* 1935, **520**, 144−150.
11. H. Dunning, J. Moore, M. Denekas, *Indust. Eng. Chem*., 1953, **45**, 1759–65.
12. H. Dunning, J. Moore, A. Myers. *Indust. Eng. Chem*., 1954, **46**, 2000–7.
13. H. Dunning, N. A. Rabon, *Indust. Eng. Chem*., 1956, **48**
14. J. Schwarzbauer, B. Jovančićević, From Biomolecules to Chemofossils. Springer, Switzerland, 2016

15. A.Treibs, *Angew. Chem.*, 1936, **49**, 682-686.

16. G. P. Dechaine and M. R. Gray*, Energy Fuels*, 2010, **24**, 2795-2808.

17. J. G. Speight, Handbook of Petroleum Analysis; Wiley Interscience: New York, 2001.

18. F. Dickson, C. Kunesh, E. McGinnis, L. Petrakis, *Anal. Chem*., 1972, **44**, 978–81.

19. K. Qian, A.S. Mennito, K.E. Edwards, D.T. Ferrughelli, *Rapid. Commun. Mass. Spectrom*., 2008, **22,** 2153–60

20. J.M Sugihara, R.M. Bean, *J. Chem. Eng. Data*, 1962, **7**, 269-271.

21. C.D. Pearson, J.B. Green, *Energy Fuels* 1993, ***7***, 338–346.

22. A. M. *McKenna* , J. M. *Purcell* , R. P. *Rodgers* and A. G. Marshall, *Energy & Fuels,* 2009**, *23*,** 2122–2128

23. H. Topsøe, B.S. and F.E Massoth, *Hydrotreating Catalysis: Science and Technology*; Springer-Verlag: New York, 1996

24. A. M. McKenna, L. J. Donald, J E. Fitzsimmons, P. Juyal, V. Spicer, K. G. Standing, A G. Marshall and R.P. Rodgers, *Energy* Fuels, 2013, **27**, 1268–1276

25. J.J. Adams, *Energy Fuels,* 2014, **28**, 2831–56.

26. O.C. Mullins, E.Y. Sheu, A. Hammami, A.G. Marshall, Asphaltenes, heavy oils, and petroleomics. Springer Science & Business Media, Berlin, 2007.

27. L. Benamsili, J.P Korb, G. Hamon, A. Louis-Joseph, B. Bouyssiere , H. Zhou., *Energy Fuels* 2013, **28**, 1629–40.

28. R. Giovannetti, in Macro To Nano Spectroscopy, ed. J. Uddin, InTech, https://www.intechopen.com/books/macro-to-nano-spectroscopy/the-use-of-spectrophotometry-uv-vis-for-the-study-of-porphyrins, Vol 1, Ch. 6, pp. 87-108. DOI: 10.5772/38797

29. C. Rimington, *J. Biochem,* 1960, **75**, 620–623

30. M. Albers and H. V. Knorr, J. *Chem. Phys.* 1941, 9

31. H. C. Longuet-Higgins*,* C. W. Rector*, and* J. R. Platt, *J. Chem. Phys*, 1950, **18**, 1174-1181.

32. M. Gouterman, 1957, *Spectrochim. Acta,* **10**, : 232-232.

33. M. Gouterman, 1961, *J. Mol. Spectrosc.*, **6,** 138

34. G. Meiyuan , H. Rongxing, D. Yulan, S. Wei, L. Ming, Z. Chaoyuan, and H.L Sheng, 2012, *J. Chem. Phys*., 136, 144313

35. L. Perrin, M.H. Perrin, M.Gouterman, *J. Chem. Phys.* 1969, **50**, 4137

36. B. Minaev, Y. Wang, C. KuiWang, Y. Luo,H. Ågren. *Spectrochim. Acta* 2006, **65,** 308-323

37. A. Gradyushko, K. Solovyov, A. Shulga, A. Starukhin, Opt. Spectrosc.,1977, **43**, 37

38. J.P. Dickie, T.F. Yen, *J .Anal. Chem*, 1967, **39**, 1847-1852.

39. S. R. Stoyanov, C.X Yin, M.R. Gray, J.M Stryker, S. Gusarov, A.J. Kovalenko *Can. J. Chem.*, 2013, **91**: 872-878

40. S.R. Stoyanov, C.X Yin, M.R. Gray, J.M Stryker, S. Gusarov, A.J. Kovalenko., *J. Phys. Chem B*, 2010, **114**, 2180-2188.

41. M. Guo, R. He, Y. Dai, W. Shen, M. Li, C. Zhu, and S. H. Lin, *J. Chem. Phys,* 2012*,* 136, 144313

42. T. M. Koper, *J. Phys. Chem. C*, 2016, 120, **29**, 15714–15721

43. J. Jiang, N. Santhanamoorthi, and C. Lo, *J. Phys. Chem. Lett.*, 2013, 4, **3**, 524–530

44. U. Even, J. Magen, and J. Jortner*, J. Phys. Chem.* 1982**, 77**, 4374

45. *U. Even, J. Jortner, J. Phys. Chem.*, 1983, **87**, 28–29

46. G. J. Van Berkel, M. A. Quinones, and J. M. E. Quirke, *Energy Fuels*, 1993, **7**, 411-419.

47. V. E. Vandell, and P. A. Limbach, 1998, J. *Mass Spec.*, **33**, 212-220.

48. T. Gozet, L.Huynh, Diethard K.Bohme. *Int. J. Mass Spec*, 2009, **279**, 113-118.

49. P. Benigni, C. Bravo, J. M. E. Quirke, J. D. DeBord, A. M. Mebel, and F. Fernandez-Lima, *Energy Fuels*, 2016, **30**, 10341-10347.

50. J. M. Beames and A. J. Hudson, *Central laser Facility Annual Report 2007/2008*, 2008, 179.

51. J. A. Wyer, and S. B. Nielsen, *J. Chem. Phys*, 2015, **133**, 546

52. S. B. Nielsen*, J. Phys. Conf. Ser*. 2012, **388**, 012026

53. C. Brunet, R. Antoine, J. Lemoine, and P Dugourd*, J. Phys. Chem. Lett.*, 2012, **3**, 698–702

54. B. F. Milne, Y.Toker, A. Rubio, A, S.B. Nielsen, *Angew. Chem. Int. Ed.*, 2015, **54**, 2170-2173.

55. M. H. Stockett, L. Musbat, C. Kjaer, J.Houmoller, Y.Toker, A.Rubio, B. F. Milne, S.B. Nielsen, *Phys. Chem. Chem. Phy.s*, 2015, **17**, 25793-25798.

56. B. F. Milne, C. Kjaer, J.Houmoller, M. H. Stockett, Y.Toker, A. Rubio and S.B. Nielsen, *Angew. Chem. Int. Ed.*, 2016, **55,** 6248-6251.

57. A.M. Buytendyk, J. D. Graham, and K. H. Bowen, *J. Phys Chem* A, 2015, **119,** 8643-8646.

58. H.L. Chen, P.E. Ellis Jr, T. Wijesekera, T.E. Hagan, S.E. Groh, J.E. Lyons, D.P. Ridge, *J. Am. Chem. Soc.* 1994, **116,** 1086−1089

59. H. L. Chen, Y.H. Pan, S. Groh, T.E. Hagan, D.P. Ridge, *J. Am. Chem. Soc*. 1991, **113**,

60. *U. Schwarz, M. Vonderach, M. K. Armbruster, K. Fink, M. M. Kappes, and P. Weis, J. Phys. Chem. A*, 2014, **118**, 369–379

61. M. Yamashita, J. Fenn. *J. Phys. Chem.*, 1984, **88**, 4451

62. N.B. Cech, *Mass Spectrom. Rev*. 2001, **20**, 362

63. L. Konermann, *J. Am. Soc. Mass. Spec*., 2009, **20**, 496

64. M. Dole, L.L. Mack, R. Hines, M.B. Alice, L.D. Ferguson, R.C. Mobley, *J. Chem. Phys,* 1968, **49**:2240–224

65. J.Iribarne, B. Thompson, *J. Chem. Phys*. 1976, **64**, 2287–2294

66. Mass Spectrometry: Principles and Applications; 2nd Ed, John Wiley & Sons LTD: Chihester, 2002

67. R.E. March, *J. Mass. Spectrom*, 1997, 32, 351

68. A. Colorado, J.Broadbelt, *J. Am. Chem. Soc. Mass Spectrom*. 1994, **5**, 1116

69. J. M. Antonietti, A. Chatelain and S. Fedrigo, *J. Chem. Phys.*, 2001, **114**, 2981-2985.

70. C. M. Choi, H. J. Kim, J. H. Lee, W. J. Shin, T. O. Yoon, N. J. Kim and J. Heo, *J. Phys. Chem. A*, 2009, **113**, 8343-8350.

71. J. C. Marcum, A. Halevi and J. M. Weber, *PCCP*, 2009, **11**, 1740-1751.

72. B. Bandyopadhyay, T. C. Cheng, S. E. Wheeler and M. A. Duncan, *J. Phys. Chem. A*, 2012, **116**, 7065-7073.

73. Y. Inokuchi, K. Soga, K. Hirai, M. Kida, F. Morishima and T. Ebata, *J. Phys. Chem. A*, 2015, **119**, 8512-8518.

74. R. C. Dunbar, *J. Am. Chem. Soc.*, 1971, **93**, 4354

75. J.D. Baldesch, *Science*, 1968, **159**, 263-&.

76. R. C. Dunbar, *J. Phys. Chem.*, 1979, **83**, 2376-2378.

77. R. C. Dunbar, H. H. I. Teng and E. W. Fu, *J. Am. Chem. Soc.*, 1979, **101**, 6506-6510.

78. R. C. Benz and R. C. Dunbar, *J. Am. Chem. Soc.*, 1979, **101**, 6363-6366.

79. J. D. Hays and R. C. Dunbar, *J. Phys. Chem.*, 1979, **83**, 3183-3184.

80. R. F. Foster, W. Tumas, J. I. Brauman, *J. Phys .Chem*, 1989, **93,** 61-68

81. D. Nolting, C. Marian and R. Weinkauf, *PCCP*, 2004, **6**, 2633-2640.

82. Horizon OPO user manual, Continuum Inc, 2012

83. W. E. Boxford and C. E. H. Dessent, *Phys. Chem. Chem. Phys.*, 2006, **8**, 5151.

84. T. F. M. Luxford, E. M. Milner, N. Yoshikawa, C. Bullivant and C. E. H. Dessent, *Chem. Phys. Lett.*, 2013, **577**, 1.

85. M. J. Frisch, G. W. Trucks, H. B. Schlegel, G. E. Scuseria, M. A. Robb, J. R. Cheeseman, G. Scalmani, V. Barone, B. Mennucci, G. A. Petersson, H. Nakatsuji, M. Caricato, X. Li, H. P. Hratchian, A. F. Izmaylov, J. Bloino, G. Zheng, J. L. Sonnenberg, M. Hada, M. Ehara, K. Toyota, R. Fukuda, J. Hasegawa, M. Ishida, T. Nakajima, Y. Honda, O. Kitao, H. Nakai, T. Vreven, J. A. Montgomery, Jr., J. E. Peralta, F. Ogliaro, M. Bearpark, J. J. Heyd, E. Brothers, K. N. Kudin, V. N. Staroverov, R. Kobayashi, J. Normand, K. Raghavachari, A. Rendell, J. C. Burant, S. S. Iyengar, J. Tomasi, M. Cossi, N. Rega, J. M. Millam, M. Klene, J. E. Knox, J. B. Cross, V. Bakken, C. Adamo, J. Jaramillo, R. Gomperts, R. E. Stratmann, O. Yazyev, A. J. Austin, R. Cammi, C. Pomelli, J. W. Ochterski, R. L. Martin, K. Morokuma, V. G. Zakrzewski, G. A. Voth, P. Salvador, J. J. Dannenberg, S. Dapprich, A. D. Daniels, Ö. Farkas, J. B. Foresman, J. V. Ortiz, J. Cioslowski, and D. J. Fox, Gaussian 09 (Revision D.01), Gaussian, Inc., Wallingford, CT, 2009.

86. L. Giacomozzi, M.Gatchell, N.Ruette, M. Wolf, G. D'Angelo, H. T. Schmidt, H. Cederquist and H. Zettergren, *Phys. Chem. Chem. Phys.*, 2017,**19**, 19750-19755

87. M. R Calvo, J .U. Andersen, P. Hvelplund, S. B. Nielsen, U. V. Pedersen, J. Rangama, and S. Tomita, *J. Chem. Phys*., 2004, **120**, 11

88. C.W. Kay, *J. Am. Chem. Soc*., 2003, 125, 13861-7

89. T. Gensch, C. Viappiani, S.E. Braslavsky, *J. Am. Chem. Soc*. 1999, **121**, 10573

90. R. R. Valiev , V. N. Cherepanov , V. Y. Artyukhov , D. Sundholm, *Phys. Chem. Chem. Phys*. 2012 **14**, 11508-17.

91. S. B. Nielsen, J S. Forster, P R. Ogilby, and S. B. Nielsen, *J. Phys. Chem. A,* 2005, **109**, 3875-3879

92. S. J. Cole, G. C. Curthoys, and E. A. Magnusson *J. Am. Chem. Soc.*, 1971, **93**, 2153–2158

93. J. A Wyer, A. V. Jorgensen, B. M. Pedersen, S. B. Nielsen, *Chem. Phys. Chem*, 2013, **14**, 4109-4113

94. J. A. Wyer, S. B. Nielsen, *Ang. Chem. Int. Ed., 2012, **51**, 10256-10260*

95. E. M. Milner, M. G. D. Nix, and C. E. H. Dessent, *J. Phys. Chem. A*, 2012, **116**, 801–809

96. T. F. M. Luxford, E. M. Milner, N. Yoshikawa, C. Bullivant and C. E. H. Dessent, *Chem. Phys. Lett*, 2013, **577**, 1-5

97. A. Svendsen, U. J. Lorenz, O. V. Boyarkin, and T. R. Rizzo, Rev. Sci. Inst. 2010, 81, 107